Summer 2022

Effects of 3D Printing on Clay Permeability

Morghan Carr
University of New Hampshire

EFFECTS OF 3D PRINTING ON CLAY PERMEABILITY

BY

MORGHAN CARR

Bachelor of Science, Louisiana State University, 2014

Bachelor of Science, University of New Hampshire, 2020

THESIS

Submitted to the University of New Hampshire

in Partial Fulfillment of

the Requirements for the Degree of

Master of Science

in

Civil Engineering

September 2022

This thesis has been examined and approved in partial fulfillment of the requirements for the degree of Master of Science in Civil Engineering by:

Thesis Director, Dr. Majid Ghayoomi, Associate Professor, Civil and Environmental Engineering

Dr. Fei Han, Assistant Professor, Civil and Environmental Engineering

Dr. Pania Newell, Associate Professor, Mechanical Engineering, University of Utah

On May 13, 2022

Original approval signatures are on file with the University of New Hampshire Graduate School.

DEDICATION

I dedicate the work within this thesis to my grandmother, Grammy, the first woman in our small family to receive her master's degree. Who has inspired me, and continues to inspire me to smile, be kind, be chatty, be curious, and *keep on keepin' on.* I also dedicate the time I've spent on this degree to my loving husband, Griffin. Who has supported me for the past seven years, but especially over the past four years, and demanded that I believe in myself-even when I didn't want to. You are my greatest blessing.

ACKNOWLEDGEMENTS

Dr. Majid Ghayoomi has been, and I imagine will continue to be, the most supportive and wonderful advisor I am fortunate enough to learn from. Thank you for encouraging me to be creative, to ask questions, and to enjoy this research. Also, thank you for gently convincing me to make the most out of my graduate school career by performing research.

I would like to thank Dr. Pania Newell, a vibrant and wonderful educator and advisor on this research. I have enjoyed, sincerely, learning from your expertise. Tangentially, I would like to thank Yanbo Wang, for his diligence in producing our 3D printed specimens and for always staying positive. Also, to Dr. Fei Han for serving on my committee, and for being an ardent and patient educator.

Thank you to the fantastic staff at the University of New Hampshire including; Noah McAdam for everything you do and educating me along the way. The UNH Instrumentation center for providing testing and imaging for our research. To Maya Norris for being a great and independent assistant researcher. Especially to my graduate student colleagues, who I look up to and have every step of the way, and have had the pleasure of getting to know you.

Finally, I would like to thank my family. Who has reaped no benefits of my schedule, who has endured my absence for birthdays, holidays, and other celebrations, and who have done so with nothing but encouragement and love. I am truly blessed beyond words and I love y'all always. Laissez les Bon Temps Rouler.

TABLE OF CONTENTS

LIST OF FIGURES

LIST OF TABLES

ABSTRACT

EFFECTS OF 3D PRINTING ON CLAY PERMEABILITY

By

MORGHAN CARR

University of New Hampshire

Advances in additive manufacturing create unique opportunities for the investigation of permeability of fine-grained soils. The permeability of fine-grained soils, such as clay, play an important role in various design considerations in the geotechnical, environmental, and stormwater management systems. Additionally, the investigations of flow through fractured clayey soils would benefit the empirical correlations that do not consider flow through macropores. This thesis investigates the feasibility of investigating permeability of 3D printed cylindrical clay specimens for the eventual application for flow through fractured clays. The effect of 3D printing, specifically direct binder jet printing, on the permeability, and other physical properties of clay was investigated. Cylindrical clay specimens were prepared using the advanced 3D printing method, direct binder jet printing, and tested in a flexible wall permeameter at effective confining stresses representing clay at very shallow depths. The results of this study show that the 3D printing process not only affects the permeability of clay, but also the specific surface area, and potentially the stiffness of the material. However, printing can provide consistent and repeatable specimens with very low disturbance and efficient controlled geometry.

CHAPTER 1

INTRODUCTION

1.1 Motivation

Fine cohesive soils, such as clays, pose challenges and opportunities in many geotechnical applications where the infiltration rate is substantially lower than that of coarse-grained soils. Cohesive soils exhibit an exponentially lower coefficient of permeability, *k*, than cohesionless soils, such as silts and sands. Such low permeability can both be a challenge or opportunity based on the engineering application. For example, the permeability of fine-grained soils influences the performance of stormwater management systems, and their ability to infiltrate rainfall (Bockhorn et. al 2017). Also, low permeability soils, such as clays, are used as geo-barriers designed to inhibit the flow of contaminants in landfills (Kozlowski, et. al. 2019) or the flow of water into landfills (Klint and Gravesen, 1999). Thus, accurate estimation of clay permeability would be crucial in the design of such systems. Further, it should be considered that permeability is a dynamic property that can be difficult to estimate due to the intermolecular properties of cohesive soils, such as clays (Das et. al, 2017).

Further, the motivation of this research is to eventually determine the effects of fractures, or crack systems, in fine grained soils and their impact on estimating permeability. The study of preferential flow through fractured clays has been investigated by many researchers (McBrayer et. al, 1997). Engineering and environmental problems related to the design of landfills liners with a compacted clay layer (CCL) are concerned with the environmental impacts of leachate infiltration into the surrounding environment due to failed CCLs (McBrayer et. al, 1997).

Preferential flow through fractured clays is also a concern in the design of stormwater management systems. Clayey soils are typically considered to be nearly impervious to stormwater infiltration (Dreelin e. al, 2006). However, the presence of fracture networks within clays can impact infiltration rate and underestimate the soils' ability to infiltrate water from storm events (Zhou, et. al, 2017). Several studies have investigated the impact of fracture networks on infiltration rate, especially through field measurements (di Prima et. al, 2020, Alaoui et. al, 2011, Abou et. al, 2010, Weiler et. al, 2003, and Sander et. al, 2007). However, there is a gap in literature in which advanced in which advanced manufacturing can be useful in determining flow through fractured fine-grained soils.

Additive manufacturing can contribute greatly to physical modeling of preferential flow through fracture geometries in fine grained soils. Determining permeability through fractured surfaces can be difficult to perform using field samples, where deformation is likely to occur during sampling, and remolding specimens for laboratory testing procedures can be difficult to control. Additive manufacturing, specifically direct binder jet printing, can create complex geometries from a wide range of materials, including clay powder, and ultimately provide a homogenous soil specimen for laboratory testing. The ability to increase the control in specimen geometry creates unique opportunities to further study the hydromechanics of soils. This research intends to test the technology and determine if direct binder jet printing is the appropriate for simulating flow through architected clay specimens. As the first step of this feasibility study, the presented work in this thesis only discuss the effects of 3D printing on permeability of solid clay specimens.

1.2 Objective/ Scope of Project

This thesis focuses on the feasibility of implementing 3D printing technologies on the investigation of clay permeability. The first step in characterizing the effects of permeability and

fracture architecture is to successfully print a 3D printed clay specimen, and to determine the impacts of printing process on clay permeability through including the physical changes experienced during printing. A commercially available clay powder designed for direct binder jet printing, composed of kaolin clay and other additives to prevent deformation during the printing process, was selected and successfully printed. Permeability tests, scanning electron microscopy, energy dispersive x-ray spectroscopy, and x-ray microscopy investigations were conducted on 3D printed specimens. The goals of this thesis are: (1) discuss the properties of soils that govern permeability (2) discuss the applications of 3D printing in geotechnical applications (3) determine the effects of 3D printing on clay permeability, and (4) determine the feasibility of implementing a pre-defined fracture geometry for future studies.

1.3 Outline

The contents of this thesis is separated into several chapters to create a fundamental understanding of the permeability of clays and additive manufacturing in the geotechnical field. The current chapter discusses the motivation of this research, an introduction to the permeability of clays and additive manufacturing, the motivation for this research, objectives and scope of the research, and the outline of the thesis.

Chapter two discusses empirical formulations for predicting permeability, and their evolution in including parameters that impact soil permeability. Two methods for measuring permeability, one in-situ method and one laboratory method are discussed to convey the benefits of measuring permeability using the flexible wall permeameter.

Chapter three provides an overview of additive manufacturing, especially direct ink writing and direct binder jet printing. Previous studies on additive manufacturing in the investigation of

soil properties are reviewed and the benefits of additive manufacturing for creating complex geometries using clay.

Chapter four describes the procedures used for investigating the effects of permeability on 3D printed clays. Material selection to fit the parameters of the ExOne Innovent+ direct binder jet printer is discussed, as well as the 3D printing procedures. Permeability testing using the GeoComp Fully Automated Set-Up is discussed, as well as sample preparation for three clay specimens to evaluate the effect of permeability at each printing stage.

Chapter five presents the results of this study. The impact 3D printing has on clay is discussed as well as the physical changes of the clay that contribute to the changes in permeability. The results include the implementation of a modified Kozeny-Carman equation to estimate the permeability of clay.

Chapter six provides the conclusions of this study and describes the benefits of additive manufacturing for future studies investigating flow through fractured clays. This chapter also recommends future work in additive manufacturing for investigating preferential flow through fractured clays, as well as further testing regarding the changes in clay due to 3D printing, such as triaxial testing.

CHAPTER 2

BACKGROUND

2.1 Soil Permeability and Theoretical Formulations

Permeability of a soil describes the rate at which fluid flows through porous media (Loudon, 1952). The coefficient of permeability in soils is a critical parameter in different geotechnical, agricultural, and environmental engineering applications, and is often obtained by either in-situ testing, laboratory measurements, or using empirical relationships. Darcy's law states that the permeability, *k*, of a soil is a function of volumetric flow, *Q*, area, *A* and the influence of an imposed hydraulic gradient, i and is expressed in units of velocity shown in Equation 2-1 (Darcy, 1856).

$$Q = A * k * i \tag{2-1}$$

Expressing permeability in terms of volumetric flow and the area over which the volume of water flows through a soil is now considered an overly simplified practice that does not account for soil specific characteristics that may impact the rate of permeability (Loudon 1952). The properties of soils often vary significantly, and external and soil specific characteristics are important to consider when estimating permeability either empirically or physically using both laboratory and in-situ methods. Hazen proposed that the grain size distribution of a soil will impact permeability. To evaluate the influence of grain size on permeability, it is important to investigate the physical properties of grain size in a soil column. Figure 2-1 shows that soil particles, like sand or other coarse grained soil types, have a larger particle size than silts or clay. The impact of particle size on permeability relates to the available void spaces created by larger particles, and it

is easily shown in the following figure that larger grained soil particles will have larger associated void spaces (Hazen et. al, 1892).

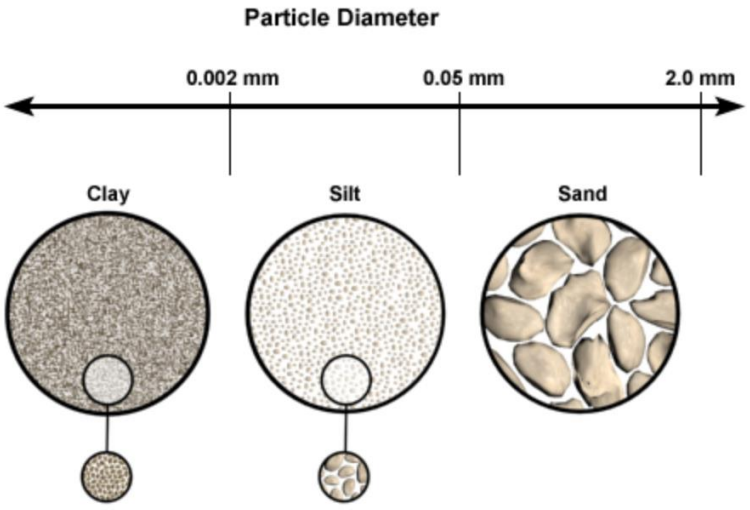

Figure 2-1 Influence of Particle Size on Void Space (The Comet Program, USDA)

In Hazens formulation of permeability, shown in Equation 2-2, permeability is only a function of the particle size the particle size for which 10 percent of the particles are smaller distribution, d_{10} (Hazen, 1892).

$$k = C d_{10}^2 \tag{2-2}$$

The associated shape constant, C, ranged from values of 41 to 146 and was typically considered to be a value of 100 (Taylor, 1948). The limitations of Hazen's formulation made the relationship unsuitable for any soils outside of sands with grain sizes between 0.1 and 3.0 mm, and soils of a uniform grain size distribution. Hazen's formula was an improvement of the work by Darcy in that the physical soil properties were considered in determining soil permeability. Based on Hazen's formula, a soil with a smaller particle size would lead to a lower coefficient of permeability, associated with the lower available void spaces in which water can easily flow. Similar empirical

formulations that include only the grain size distribution of the soil were proposed by Slichter in 1899, shown in Equation 2-3 (Slichter, 1899). The constant, c, was considered a function of the porosity of the soil and determined through curve fitting, where porosity is considered as the volume of void space divided by the total volume of a soil element shown in Equation 2-4, and d_s is the effective grain size, an improvement in eliminating yet another unknown variable that may govern flow through soil, and determined by curve fitting of experimental permeability results.

$$k = \frac{771 d_s}{c} \tag{2-3}$$

The effectiveness of determining soil permeability for correlations that include soil particle size was verified to be an acceptable determination of permeability by many studies, including those by Shlichter (1899), Schriever (1930), and Burmister (1954), to name a few (Chapuis, 2003). Grain size correlations for the purpose of determining permeability were verified by performing laboratory tests on unconsolidated soils (Berg et. al 1986).

$$e = \frac{V_{voids}}{V_{solids}} \tag{2-4}$$

However, the effects of void ratio, on soil permeability were investigated by Taylor et. al. (1948), and it was determined that decreasing the void ratio through confining pressure will also decrease the coefficient of permeability, shown in Equation 2-5.

$$k = C \frac{e^3}{1+e} \tag{2-5}$$

Taylor expressed permeability in terms of a shape function, C, and the void ratio, *e.* The shape function, C, may be a constant or will vary as the void ratio varies, and is determined by Equation 2-6.

$$C = C_s \frac{\gamma_w}{\mu} \frac{1}{S_o^2} \tag{2-6}$$

Taylor's formulation for permeability expresses permeability not only in terms of void ratio, but also considers the physical properties of the fluid, such as dynamic viscosity, μ, and unit weight, γ_w. Notably, specific surface area, S_o , and a function of the particle size distribution is present in Taylors formulation as well as the shape factor, C_s to account for some physical properties of the soil in permeability, an improvement upon formulations that only account for soil grain size. Figure 2-2 displays that an increase in void ratio for a certain soil type will increase the permeability of the soil. Such relationships are important to consider to estimate the rate of consolidation for low permeable soils which incorporate the void ratio for soils under consolidation, as well as to estimate permeability.

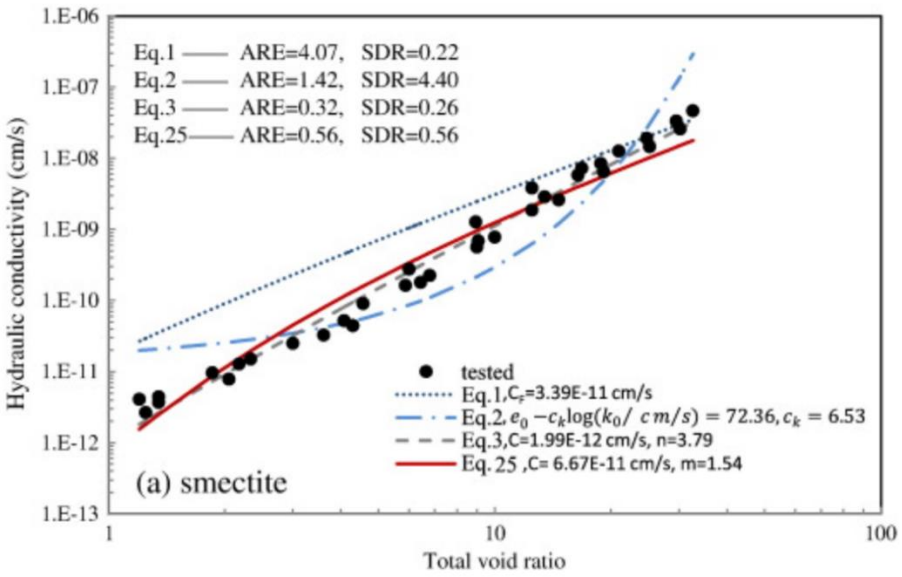

Figure 2-2 Relationship Between *e* and log *k* (Ren et. al, 2016)

Perhaps the most commonly used empirical formulation for determining permeability was introduced by Kozeny (1927), and later improved upon by Carman (1937) (Chapuis et. al, 2003). What is now referred to as the Kozeny-Carman formulation was developed upon a derivation of the Navier-Stokes equation, where soil was considered to be a set of capillary tubes leading to a function to include the void ratio, *e*, the specific surface area, *S*, the shape factor, C, and the specific weight *Dr*, or the ratio of the density of the soil solids to the density of water. The Kozeny-Carman equation also considered the properties of the permeant, usually water, and included the dynamic viscosity and unit weight of the fluid, a variation of this relationship is shown in Equation 2-7.

$$k = C\frac{g}{\mu_w p_w}\frac{1}{S_0^2\, D_r^2}\frac{e^3}{e+1} \qquad (2\text{-}7)$$

Two parameters absent from previously shown formulations include the specific surface area as well as the specific weight of the soil. While the Taylor formulations do show that grain size will affect the coefficient of permeability, the formulation does not consider the specific surface area which is a function of the particle size and shape. The specific surface area of a soil is defined as the total surface area of soil particles per unit mass (Holtz et. al, 2011). Fine-grained soils, such as silts and clays, have higher specific surface area than sands or gravels for a soil column of equal dimensions. Increased specific surface area of a soil mass will account for larger particle interaction within a soil column, where smaller particles will create less available void spaces as they are packed together (Campbell et. al, 2013). Specific surface area has historically been determined by lengthy and complex analytical methods, or estimated from theoretical equations (Duriez and Arrambide, 1962). Tangentially, a more appropriate method of determining the specific surface area, in units of $\frac{m^2}{kg}$, of a soil is performed utilizing the grain size distribution

(Chapuis et. al, 1992). For non-cohesive soils, the specific surface area can be estimated using Equation 2-8 (Chapuis et. al, 1992).

$$S = \frac{6}{dp_s} \tag{2-8}$$

Equation 2-8 relates specific surface area to the density of the solid particles, p_s, and the particle size diameter, *d.* Expanding upon Equation 2-8, Chapuis et. al (1992) proposed Equation 2-9 to determine specific surface area for non-cohesive soils, where $(P_{No\ D} - P_{No\ d})$ is considered as the difference of the percentage by weight smaller than a defined particle size, D, and the next larger size, *d*.

$$S = \frac{6}{dp_s}\Sigma(\frac{P_{No\ D} - P_{No\ d}}{d}) \tag{2-9}$$

Chapuis' improvement to the specific surface area determination accounts for the entirety of the grain size distribution. Table 2-1 displays sample calculations for this method using grain size curves provided by Craus and Ishai (1977) (Chapuis et. al, 2003). The specific surface area of this particular limestone fill was determined to be 325.2 $\frac{m^2}{kg}$.

Table 2-1 Specific Surface Area for Limestone Filler (Chapuis, 2003)

Size (mm)	Cumulative passing (%)	Difference X ($P_{No\ D} - P_{No\ d}$)	$S = 6/d\rho_s$ (m^2/kg)	XS (m^2/kg)
0.074	100	—	—	—
0.06	94	0.06	34.72	2.08
0.05	89	0.06	41.67	2.08
0.04	83	0.06	52.08	3.13
0.03	76	0.07	69.44	4.86
0.02	65	0.11	104.17	11.46
0.01	45	0.2	208.33	41.67
0.005	24	0.21	416.67	87.5
$d_{eq.} = 0.0029$		0.24	718.39	172.41

However, the limitations of the Kozeny-Carman formulation as presented in Equation 2-7 has been shown to be invalid for cohesive soils (Carman et. al, 1937). This limitation further complicates predicting the permeability of plastic and cohesive materials, as the provided specific surface area estimations (Equation 2-8 and Equation 2-9) are also inaccurate for plastic soils.

2.2 Estimating Permeability of Cohesive Soils

Estimating the permeability of cohesive soils has been investigated by many researchers (Chapuis et. al, 1992, 2003; Lamb et. al, 1969; Samashiringhe et. al, 1972; Terzaghi et. al, 1925; Zunker, 1932), and generally is considered to deviate from Darcian flow. Thus, investigating the properties of clays is paramount in determining proper estimations of their permeability.

The aforementioned discussions have shown that flow through porous media is a function of various mechanisms and is especially variable when considering the permeability of cohesive soils. Clay permeability is not only influenced by its particle structure (Chen, et. al. 2019), but also by its high specific surface accompanied by electric charges (Mitchell and Soga, 2005), its ability to adsorb water molecules, a polar molecule, through the formation of the electric diffuse double

layer (EDL) (Mitchell and Soga, 2005), and particle shape and pore size and distribution effects (Chen et. al. 2019). Soil is typically a three-phase media in field conditions, with solid soil particles, water, and air (for unsaturated conditions) and are a two-phase media for saturated soils, with only soil particles and water. The intrinsic ability for clay to adsorb water complicates the two or three phase media definition as it pertains to the evaluation of available void spaces, or pore spaces. The EDL, a characteristic which is specific to cohesive soils, inhibits flow of fluids through pore spaces by reducing the void ratio due to the adsorption of water to clay particle. Therefore, the available voids in which a fluid can flow is further constricted in cohesive soil and Equation 2-4 should account for the available void spaces in clays, such that Equation 2-10 is introduced for saturated conditions (Le et. al, 2019; Taylor, 1948). Figure 2-3 displays the phase diagram of a saturated clay specimen and notably the presence of an adsorbed water layer, or unfree water (Le et. al, 2019).

$$e = \frac{V_{voids}}{V_{solids} + V_{adsorbed\ water}} \tag{2-10}$$

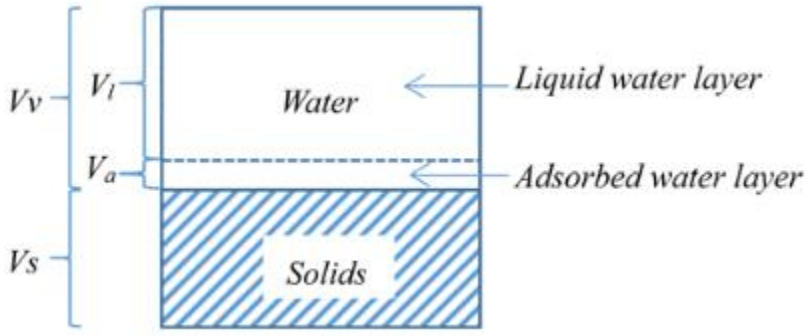

Figure 2-3 Diagrammatic representation of soil as a two-phase system, showing free water layer and unfree water layer (Le et. al, 2019)

The presence of the EDL most notably is shown to cause clay materials to exhibit cohesion, plasticity, and in some cases, swelling (Moore et. al, 1991; Wienberg, 1990). While there are segregated conclusions on the total effect of the EDL on clay materials, such as the magnitude of cohesion and plasticity (Moore et. al, 1991 and Powrie, 1997), a generally acceptable consensus is that the presence of the EDL in clays does affect the coefficient of permeability (Schmitz, 2004). Thus, in terms of estimating permeability in clay, especially using the Kozeny-Carman formulation, it is important to include acceptable measurements of specific surface area and other shape functions based on the underlying properties of clays. Several empirical and theoretical relationships have been proposed to determine the permeability of clays (Li et. al, 2019). In general, the permeability of cohesive materials is dependent upon several factors including plasticity, void ratio, and specific surface area. Regarding plasticity, permeability of clays is shown to decrease while plasticity increases (Dolanir, 2004). Terzaghi (1925) was first to introduce a relationship to predict the permeability of clays using Atterberg Limits. Since then, other empirical relationships were introduced to calculate the expected permeability of the soil, mainly utilizing the void ratio after permeability testing was completed. For example, the relationship shown in Equation 2-11 estimates the hydraulic conductivity of normally consolidated remolded clay specimens (Samarasinghe et. al, 2000).

$$k = \frac{C e^{x}}{1 + e} \tag{2-11}$$

Where *e* is the void ratio, *C* and *x* are permeability constants determined experimentally, for clay soils, with a low swelling index (Samarasinghe et. al, 2000). The constant C is a shape function determined from Plasticity index using Equation 2-12.

$$C = 0.00104 PI^{-5.2} \tag{2-12}$$

Chapuis et. al (2003) introduced an extension of the Kozeny-Carman formulation by defining the specific surface area of clays as a function of their Atterberg limits, as shown in Equation 2-13.

$$\frac{1}{S} = 1.3513\frac{1}{LL} - 0.0086 \qquad (2\text{-}13)$$

The application of the liquid limit to determining the specific surface area resulted in reasonable predicted coefficients of permeability for cohesive soils. The estimations of specific surface area used in the study by Chapuis et. al (2003) were applicable in the following extension of the Kozeny-Carman formulation as shown in Equation 2-14 below.

$$log\ (K) = A + log\ (\frac{1}{S_0^2\ D_r^2}\frac{e^3}{e+1}) \qquad (2\text{-}14)$$

Chapuis' extension to the Kozeny-Carman equation was verified for both cohesive and non-cohesive soils using permeability data published by multiple investigators, such as Mesri and Olsen (1971), Mavis and Wilsey (1937), Loiselle and Hurtubise (1976), to name a few. Theirstudy found that the Chapuis' extension in determining specific surface area fits well with the log value of permeability and can be used for quick estimates of the coefficient of permeability for field investigations, and can be used for verifying laboratory test data (Chapuis et. al, 2003). The limitations of this formulation are discussed as follows. The soil permeability prediction is reasonable for naturally homogeneous soils; it will confidently estimate the value of *k* of any soils falling within the permeability range of $10*10^{-1}$ m/s to $10*10^{-11}$ m/s. One of the largest contributions of dispersion in permeability data, as Chapuis noted, in a discussion written in 2012, is improper sample preparation, and improper determination of the specific surface area. For the

purposes of this study, Chapuis' extension to the Kozeny-Carman equation is used to estimate specific surface area as 3D printed clay specimens undergo various procedures from raw manufactured clay powder, to a complete 3D printed specimen; thus, changes during the process may impact the coefficient of permeability.

2.3 Physical Measurements of Permeability

The coefficient of permeability of a soil can be determined using several methods. Mathematical formulations are used to estimate the permeability of a soil using known or estimated physical properties of the soil and the permeant. Field testing methods attempt to determine the in-situ permeability of a soil and are often very expensive and time consuming to perform. Laboratory methods are most commonly used, but require a significant amount of sample disturbance, and then subsequent reconstitution of specimens to simulate field conditions in a laboratory setting (Lefevbre, 2021). While this study does not perform in-situ permeability testing, it is important to note the advantages and disadvantages of each method for a feasibility study. This section describes one common field and one common laboratory test that can accompany theoretical estimations of permeability.

2.3 Field Infiltration Tests for Soil Permeability

Infiltration tests are commonly used by field investigators where the driving advantages are their simplicity, time effectiveness and they are typically the least expensive field test to perform.. Infiltration tests are performed in a drilled borehole, where a casing is placed atop an added layer of permeable material (such as gravel or coarse sand) to prevent disturbance of the top layer by the addition of water. The casing is then typically surrounded by a swelling clay, such as bentonite, to prevent lateral seepage from the borehole. A volume of water is introduced to the borehole, and infiltration rate is determined by measuring the drop height of water in the casing

over a period of time, and applying empirical shape factors of the casing (Hvorslev, 1951). This method closely resembles the falling head test performed in laboratory environments, and does require some evaluation of empirical formulations to determine the coefficient of permeability. There are many disadvantages of the infiltration test, such as appropriate weather conditions, the impact of soil inhomogeneity, the application of empirical formulations to determine permeability, as well as potential soil disturbance during installation of the casing (Lefebvre, 2021).

2.4 Flexible Wall Permeameter Tests for Soil Permeability

The flexible wall permeameter test is a laboratory test designed to determine soil permeability by reconstructing field conditions within a test cell, often used in a modified triaxial system set up. A set up by GeoComp Load Trac II load frame, accompanied by three Flow Trac II flow pumps, found at the University of New Hampshire Soil Mechanics Laboratory has been used in this research and is shown in Figure 2-5, which is also discussed in this section.

Figure 2-4 GeoComp Permeability Test Set Up (GeoComp).

Flexible-wall permeability tests are performed on soil specimens, either reconstituted, or from relatively undisturbed samples from the field. An advantage of using flexible wall permeability is the customization of the specimen size availability within the triaxial test cell due to interchangeable top caps and bottom pedestals, which lessens the need for trimming field samples or reconstitution. Specimens are placed between filter paper and porous stone at the top and bottom surfaces, and within an impermeable flexible membrane, often latex in material. Specimens are then placed on the bottom pedestal and secured to the top cap with an O-ring. Samples may be prepared using various methods of reconstitution. Coarse grained materials are typically prepared to a relative density via dry pluviation, to simulate certain field conditions determined by the investigator, and cohesive materials are typically reconstituted through various methods of compaction (Ladd, 1978). A typical test cell set up is shown in Figure 2-6 below, of the triaxial test cell at the University of New Hampshire. With the specimen prepared on the bottom pedestal, as shown in the figure, the triaxial test cell is then filled with de-aired water, used to apply confining pressures to the specimen.

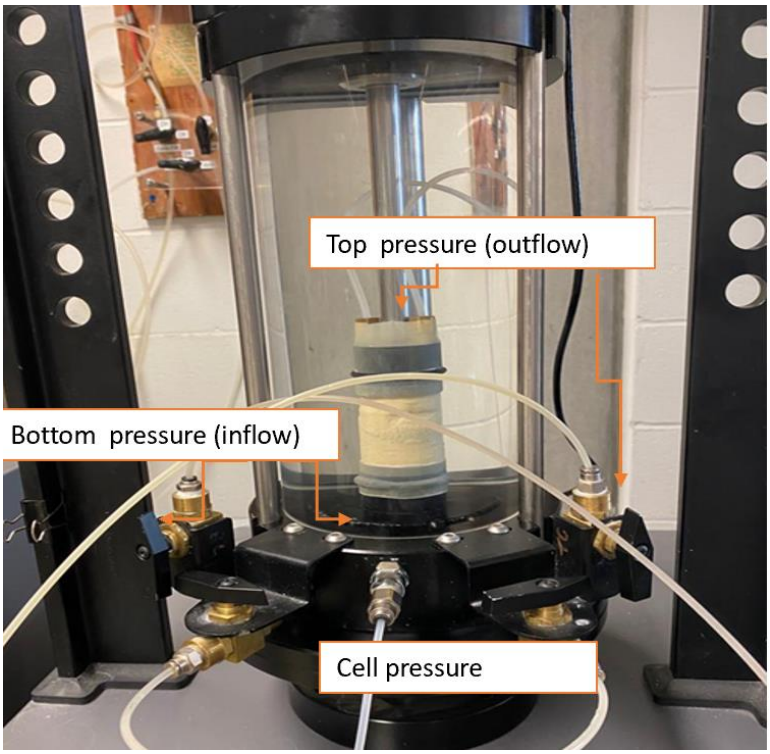

Figure 2-5 Flexible Wall Permeameter (University of New Hampshire)

Drainage lines are located at the top and bottom pedestals and promote drainage through the specimen, required during the stages of the permeability test. An array of permeants may be used in the flexible wall permeability test, however the most common permeant is typically de-aired water (Daniels et. al, 1985). The double drainage lines at the top and bottom pedestals are especially important during the saturation stage of the permeability test, which will be discussed in the latter portion of this section. The use of de-aired water ensures pressure changes are accurately measured, as water is considered to be an incompressible material, and the presence of air within the system will impact pressure drop measurements, confining pressure measurements, and porewater pressure measurements within the specimen and within the test cell (Daniels et. al,

1985). The GeoComp system shown in the figures is a fully automated testing system, requiring no intervention beyond sample preparation.

The flexible wall permeability test is performed in three stages after an initialization phase, including saturation, consolidation, and permeability. Constant flow and constant gradient tests are typically performed in the flexible wall permeability test, and the constant gradient flow test is discussed in this section. The initialization phase allows the investigator to observe any sample preparation or equipment error within the test cell, most notably, leaks within the pressure lines or membrane that are not visible to the observer. A small confining pressure and pore pressure is applied to the specimen, through the test cell chamber and bottom pressure, respectively. The effective stresses at this stage must never be greater than the effective stresses performed during the permeability test, to prevent overconsolidation. Significant changes in volume indicate equipment damage and prevent inaccurate results during the permeability test if performed properly.

Permeability tests are performed on fully saturated specimens, where backpressure saturation is performed by the application of confining stress via de-aired water within the test chamber and the introduction of porewater pressure through the bottom pedestal. The confirmation of saturation is determined through a B-value determination, shown in Equation 2-15 where Δu is the change in porewater pressure and $\Delta\sigma_3$ is the change in confining pressure. Soils that are completely saturated will have a B-value of 1.0; however, a value of 0.95 to 1.0 is considered acceptable for the purposes of the permeability test.

$$B = \frac{\Delta u}{\Delta \sigma_3} \tag{2-15}$$

Consolidation is performed once an acceptable B-value is reached, and the specimen is saturated. Effective stress, shown in Equation 2-16, that is applied to the specimen is determined based on either the field conditions or at the discretion of the tester.

$$\sigma'_3 = \sigma_3 - u \tag{2-16}$$

The effective stress, σ'_3, describes the stress, or pressure, the soil particles are exposed to. Assuming water is incompressible, porewater pressure will resist the effects of total confining pressure, σ_3, leaving the difference between the two pressures as the pressure that will impact the soil specimen. The sample will be consolidated under the target effective confining stress.

The final stage of the flexible wall permeability test is the constant gradient or constant flow permeability test, where the constant gradient test is used in study and discussed in this section. Permeability is measured by applying a hydraulic gradient through the bottom pedestal to the saturated and consolidated specimen. The hydraulic gradient will allow water to flow through the saturated specimen, and flow is measured through the top cap. Selecting a hydraulic gradient for a specimen will depend on the effective confining stresses applied to the specimen during consolidation that are held throughout the constant gradient test. Higher confining pressures will require a higher hydraulic gradient to be applied to the specimen, such that the permeant may flow to reach steady state flow. Steady state flow is determined as the equivalence of flow applied through the bottom pedestal and measured out the top cap and should be determined as such at an equivalence of approximately 5-8% (Chapuis, 2012). A disadvantage of the flexible wall permeameter is the application of a hydraulic gradient that is large enough to measure flow at high confining pressures. Daniels et. al (1985) discusses that the pressure drop across a specimen from an applied gradient must not be larger the effective confining pressure. However, at very low

confining pressures, the hydraulic gradient must be very small and accompanied by a very small pressure drop from one end of the specimen to the other. Therefore, identifying an applicable confining pressure should be associated with determining the lowest possible hydraulic gradient needed to achieve steady state flow, and accurately measure permeability.

CHAPTER 3

3D PRINTING APPLICATONS

3.1 Introductions to 3D Printing

Additive manufacturing applications create unique opportunities in the investigation of in-situ soil behavior due it its capacity in producing structurally controlled specimens with similar characteristics. Specifically, additive manufacturing of cohesive soils provides a chance to prepare clay specimens with controlled void ratio, and potentially fracture geometry, to observe flow through fractured clays. Further, binder-jet 3D printing of clay samples can be beneficial in studying the interaction of micro-fractures commonly found in low permeable soils, which may dictate the flow. In-situ permeability testing of cohesive soils are expensive and rely on estimations of the geometry of the soils as well as the boundary conditions (Pap et. al, 2019). Further, laboratory testing of samples obtained from the field may also be impacted by sample disturbance that occurs when removing the confining pressures of the specimen during extraction. Thus, existing microfractures may be disturbed, which in turn can affect the coefficient of permeability. Therefore, 3D printed clay specimens introduces a new path in investigating flow through microfractures in cohesive soils and their effects on permeability. There are many forms of 3D printing, and two specific forms of printing are discussed in this section, both with applications in the geotechnical field including direct ink writing and direct binder jet printing.

3.2 Direct Ink Writing

Direct ink writing (DIW) is the most common form of 3D printing. This method is used in a myriad of applications including the manufacturing of batteries, catalytic systems, ceramic applications, and at a large scale, even buildings (Ordones et. al, 2019, Tagliaferri et. al, 2021). Direct ink writing is an extrusion-based printing method that requires the printing medium to be

deposited in a slurry (Lewis et. al, 2006). DIW was introduced at the Sandia National Laboratories in 1997 with the intention of fabricating complex geometrical prints using ceramic pastes (Cesarani et. al, 1997). DIW builds complex geometries by extruding a material slurry at room temperature, with the ability to easily print ceramic type slurries that allow them to retain their shape during the extrusion process. Layers of material are printed atop one another in sequence through an extrusion nozzle, where print geometry is created through common computer aided design programs, such as AutoCAD 3D (Shahzad et. al, 2021). Once a successful print has been completed by DIW, the specimen must be sintered, a process in which the specimen is heated at very high temperatures to ride the print of the binder used in the slurry to help the material maintain its shape. Binder components used in DIW are typically organic or polymer-based binder fluids (Shahzad et. al, 2021). Figure 3-1 displays a typical DIW process by extrusion.

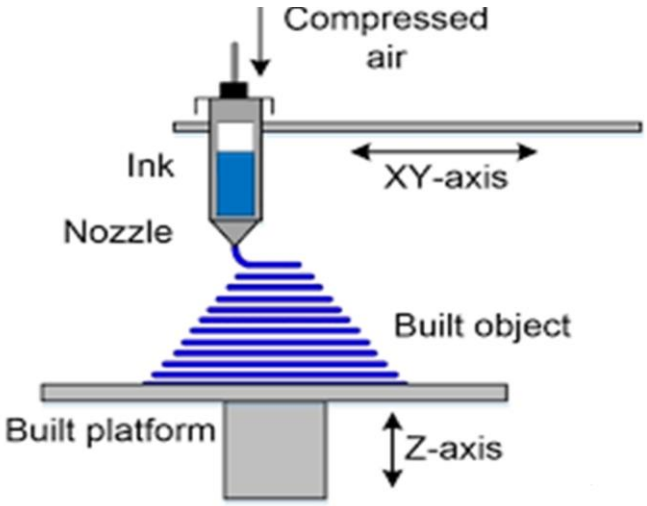

Figure 3- 1 Schematic of Typical DIW Procedure (Pinargote et. al, 2020)

Determining appropriate material properties that will adequately flow is required to successfully print via DIW. Various nozzle sizes and shapes, printing speeds, and sintering methods will impact the preparation method for the appropriate viscosity of the printing medium. Slurry preparation, for ceramic prints, is performed by mixing ceramic-clay powder in de-ionized water. Other additives are used for increasing the flowability and other mechanical properties of the slurry and produce a homogeneous mixture that is free of air. The slurry must be prepared at such a viscosity that allows both flowability, as well as maintain enough strength to hold its shape once it is extruded (Samay et. al, 2002). There are many benefits in industry to DIW for ceramic parts, and the larger range of particle size diameter of the clay powders used to create the prints is an added benefit offering a variety of raw material selection. However, the DIW process is less suitable for the introduction of internal fracture geometries requiring a layer of material to be freestanding within the print and carry the weight of the subsequent prints. Deformation will likely occur during the printing process and be exacerbated during the sintering process. It is very common for the formation of defects to occur during the sintering process of DIW prints, this is typically due to the evacuation of the binder and additives causing shrinkage of the part and promoting cracks within the geometry (Deckers et. al, 2014).

DIW has been used in many studies to investigate the mechanical properties of ceramic or clay-based materials, in geotechnical, environmental, and material science fields. A study by Tang et. al (2020) implemented DIW to investigate the microstructure of functionally graded materials, kaolinite and barite mixtures, to model the Chinese Majiagou landslides. However, a large majority of studies on the application of DIW using clay or ceramic powders are procedural studies to determine the appropriate rheological properties of the printing medium, binder, and additives to

produce quality prints (Christ et. al, 2015; Lewis et. al, 2006; Revelo et. al, 2019; Travitsky et. al, 2014; Xia et. al, 2016).

3.3 Direct Binder Jet Printing

Direct binder jet printing differs from the extrusion based DIW methods in its ability to print complex geometrical shapes using a material powder, such as ceramic-clay powders. Unlike DIW, there is little to no material preparation in terms of creating a slurry which eliminates a considerable amount of complexity to create a 3D printed object. Direct binder jet printing creates complex geometries by rolling or spreading a thin layer of material powder to a flat surface, or powder bed, and then selectively injecting a binder material in the predetermined geometry. This process is repeated until the final product is printed, at which point the printed material is extracted from the powder bed. A successful print will then be sintered, or heated at very high temperatures, to both expel the added binder, and cure the part. Figure 3-2 displays the typical procedure for direct binder jet printing.

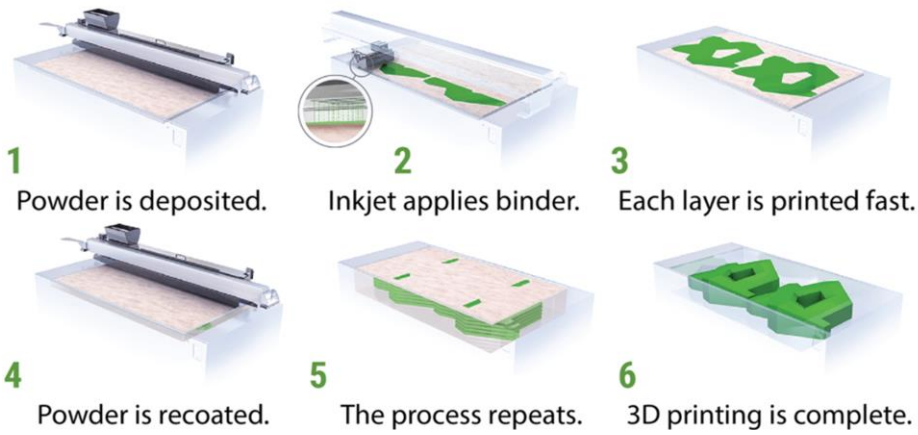

Figure 3- 2 Schematic of Typical Printing Procedure for Direct Binder Jet Printing (exone.com)

While both methods of additive manufacturing discussed in this section are advantageous in their ability to reduce material waste, direct binder jet printing is more efficient in the use of the printing medium than DIW methods where the leftover material in the powder bed may be used for a new print.There are many commercial manufacturers of direct binder jet printers. This study utilized the Exone Innovent + printer located at the University of Utah in Salt Lake City, UT, shown in Figure 3-3 below.

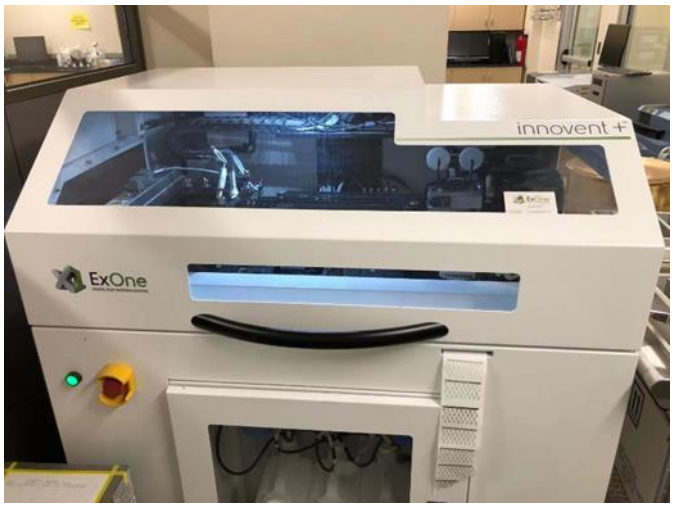

Figure 3- 3 Exone Innovent+ Direct Binder Jet Printer, University of Utah

While material preparation is simpler for binder jet applications than DIW, the properties of the printing medium are especially important (Hanoar et. al, 2016). Material flowability, referring to the powder medium, is mostly a function of its particle size and particle shape, and can also be affected by temperature and moisture (Hanoar et. al, 2016). In terms of particle shape, clay powders used for ceramic prints are commonly found in both round and angular shapes (Lv, et. al, 2019). The flowability of a printing medium will impact its ability to be spread evenly across the powder bed, during the powder deposition stage of 3D printing. Consequently, if the

flowability does not produce even layers across the spread, defects due to an imbalance of material throughout a print may occur (Lv et. al, 2019). The effect of poor flowability on clay powders used for 3D printing can be improved by many methods including controlling the particle shape, and frequently by the use of additives designed to increase flowability (Spillman et. al, 2010).

Direct binder jet printing is also influenced by the material bulk density, which will impact the material composition of the parts during the printing process. There are two properties of the material that should be considered for print performance during printing, and subsequently during sintering: the bulk density and the sinterability. The bulk density of the material is considered as the bulk density of the green body, or the printed part with binder before sintering occurs. This bulk density will impact the sinterability of the specimen, which is largely due to the compaction and densification during the sintering phase (Lv et. al, 2019). Finally, particle shape and particle size are important to consider when selecting a printing medium (Chiangka et. al, 2016; Jallo et. al, 2010). These parameters will largely depend upon the type and model of the printer used to create 3D parts, however, as mentioned the flowability of the material will also be impacted by particle shape. Typically, rounded particle shapes are considered the optimal choice for flowability, however during printing process, the particles are slightly compacted due to the roller spreading new material atop the freshly deposited binder (Lv et. al, 2019). Rounded particles have been shown to have less compaction than angular shaped particles, with a much lower packing density (Smale et. al, 2012). Particle shape will also impact sinterability, according to a study performed by Suwanprateeb et. al (2018), where angular shaped powders produced parts with higher densities after sintering than the rounded powders. Particle size is also important to consider and may be one of the larger challenges in selecting a material, such as clay, for direct binder jet printing. Typical particle sizes for various printers are usually no greater than 200 μm and no less

than 0.2 μm (Feenstra et. al, 2005; Spillman et. al, 2010; and Nebelung et. al, 2009). For example, the minimum particle size for the Exone Innovent + printer is 4 μm, which falls within the range of soils classified as a clay. Each of the discussed limitations of the particle size should be carefully considered when selecting a powder, although clay powders manufactured for direct binder jet printing are becoming increasingly common.

Binder jet printing is an excellent way of creating geometries that are more complex than that of DIW printing. Figure 3-4 below prints performed by Revelo et. al (2021) using DIW methods, and Figure 3-5 displays printed specimens using direct binder jet printing by Chen et. al, (2022).

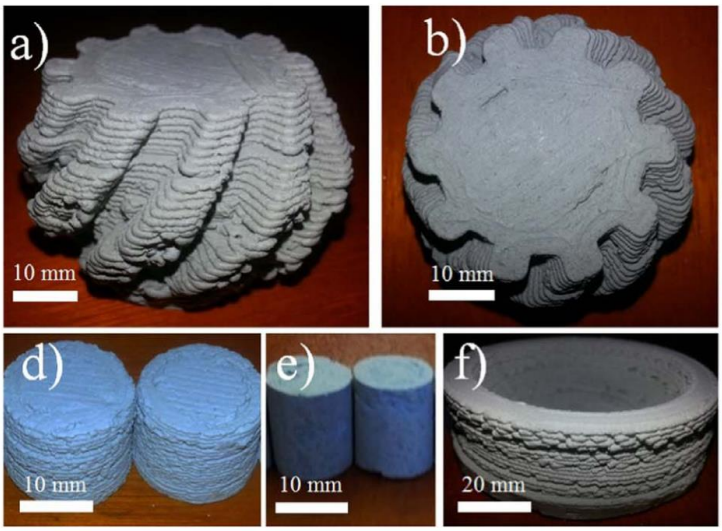

Figure 3- 4 Complex Geometries of Ceramic Prints by DIW (Revelo et. al, 2021)

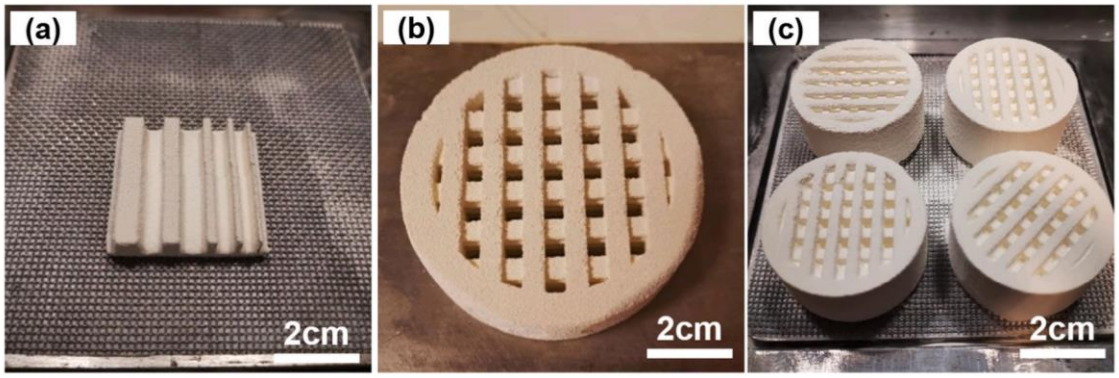

Figure 3- 5 Complex Print Geometries by Direct Binder Jet Printing (Chen et. al, 2022)

Perhaps the most notable difference in the quality of the prints performed by DIW and binder jet printing is the elimination of visible extrusion layers left by DIW. As previously stated, the motivation of this study is to ultimately introduce a predefined finite fracture geometry into cylindrical 3D printed clay specimens. Specimen geometry, at minimum, is the driving factor in producing a quality specimen to study of the effects of 3D printing on clay permeability and other properties of clay, as well as the study of flow through macropores or fractures. Thus, direct binder jet printing is the most reasonable and preferred method.

3.4 Recent Works in Direct Binder Jet Printing with Geo-Applications

The applications of additive manufacturing in geomaterials are not limited to a soil-based printing medium. In fact, most 3D printing studies that implemented direct binder jet printing were performed using polymer-based powders as the printing medium. In recent years, 3D printing of soil particles using artificial and natural materials has been applied to non-cohesive soil types (Gomez et. al. 2019) as well as rock structures (Jiang et. al. 2020). However, few studies have been performed investigating the application of direct binder jet 3D printing to investigate transport and mechanical properties of cohesive soils (Tang, 2020). Thus, it is reasonable to apply

technologies in additive manufacturing, especially direct binder jet printing, to printing mediums that are made of soil type material- such as clay or sand.

A study performed by Hanoar et. al (2016) utilized direct binder jet printing to print singular soil particles, representing a granular material, by using a cured polymer as the printing medium. This study sought to identify a printing medium with similar physical properties, such as specific gravity and elastic modulus, that closely resembles quartz, which they ultimately selected Fullcure 720 resin by Stratasys, USA. Designing and fabricating reasonable particle shapes were determined based on two methods, of which were ultimately converted into CAD drawings to generate the printed granular material using the Objet Eden 250 poly-jet type 3D printer. Two numerical models were selected for the particle geometry design as the fractal surface overlay (FSO) and counter rotation interpolation (CRI). Artificial soil particles were subsequently printed and then investigated based on their print quality and were ultimately tested under triaxial conditions to determine if this method is applicable to the investigation of coarse-grained materials. Figure 3-6 below displays comparisons of printed grains versus simulated grains using the FSO modeling method.

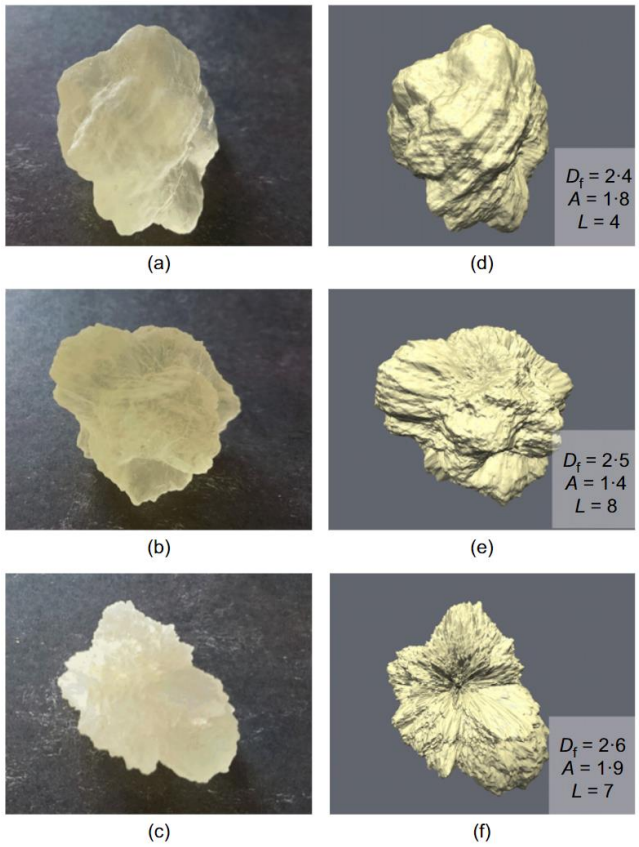

Figure 3- 6 Comparison of Printed (a, b, c) Granular Material versus FSO Simulated (d,e,f) Granular Material

The printed granular material was then tested under drained triaxial conditions at an effective confining stress of 20 kPa. They stated that the selection of the low confining stress was reasoned to be comparable to the effect of a 1MPa confining stress on a specimen made of quartz. Figure 3-7 below shows the results of the drained triaxial tests performed in the study, where specimens were prepared by loosely placing the printed particles and tamping in a cylindrical form.

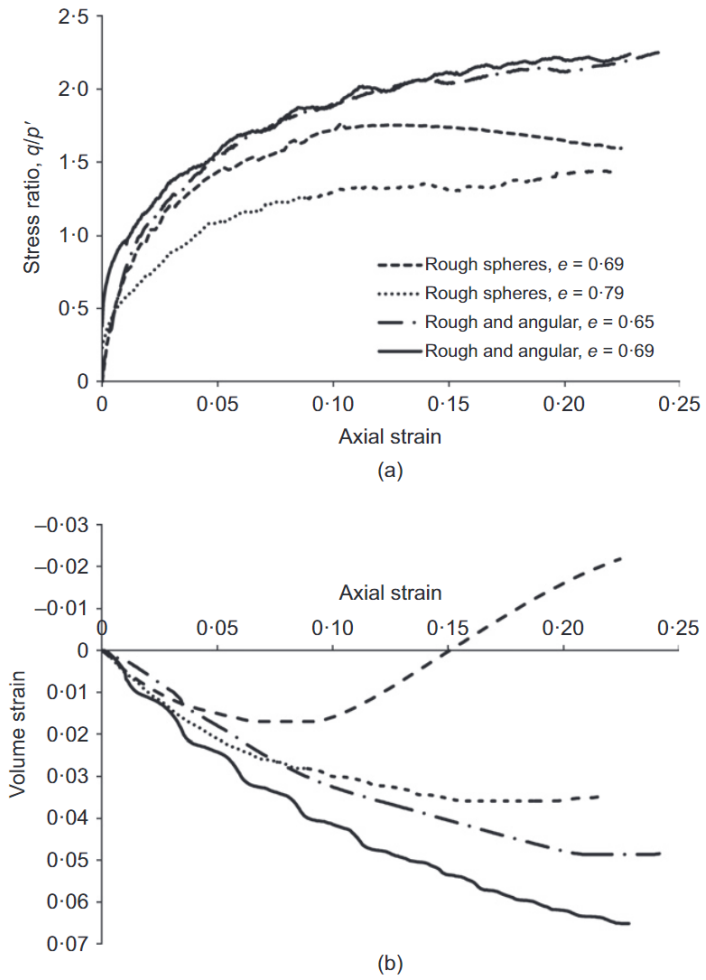

Figure 3- 7 Triaxial Behavior of Printed Grains (Hanoar et. al, 2016)

The results of the triaxial tests performed on the printed granular material were consistent with the shearing behavior of sand, especially for the rough shaped particles. They stated that the peak of the shearing behavior in the stress ratio space for the denser prepared grains, and subsequent decrease in stress ratio is a reasonable behavior of a densely prepared sand specimen. Additionally, the dilative behavior of the denser rough shaped grains, was consistent with the behavior of granular material. Nevertheless, the compressional response of the material was

determined to be more compressible than seen in sandy or granular material, and was determined that the printing medium was more compressible than a sandy soil.

A study by Wei et. al (2021) built upon the work of Hanoar et. al (2019) used the same printer and material to print coarse-grained particle shapes from scans of actual aggregates. Their study included nine aggregate types obtained from the Virtual Cement and Concrete Testing Laboratory, Leighton Buzzard sand, granite from a previous study (Wei et. al, 2018), and Ottawa sand, shown in Figure 3-8. The purpose of their study was to demonstrate the applicability of a modified Kozeny-Carman equation by printing uniformly graded material with various associated irregular shapes.

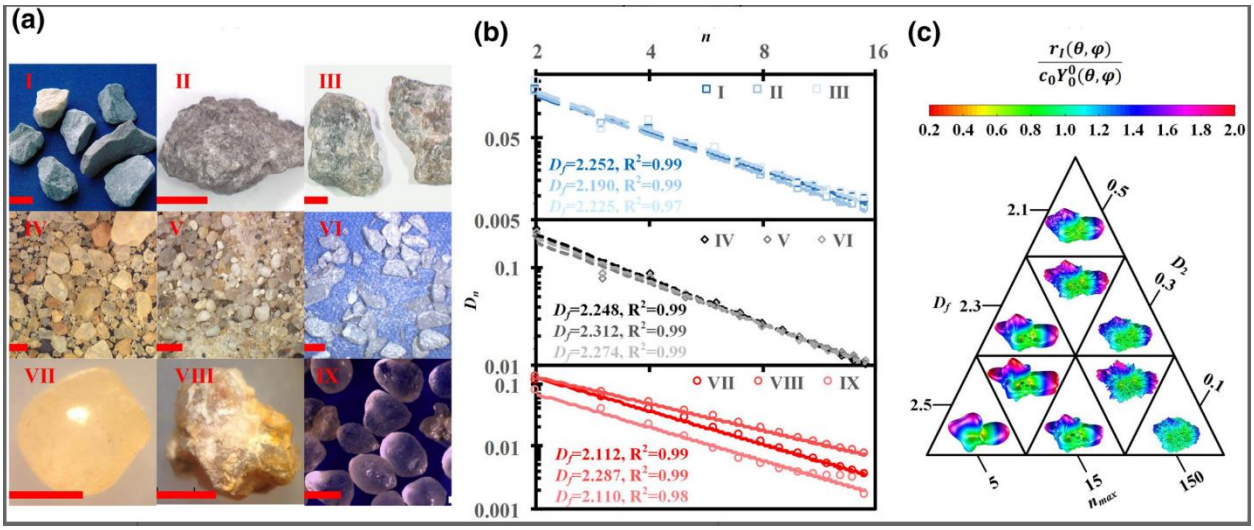

Figure 3- 8 Aggregates and Sand Particle used for Surrogate Granular Material in 3D Printing (Wei e. al, 2021)

(Wei et. al, 2018) sought to determine if particle shape will also influence the coefficient of permeability. Printed soil grains were prepared at different void ratios where each specimen was comprised of either spherically shaped particles, or various degrees of angularity defined as, D_f.

A D_f value of 2.1 is considered angular and a value of 2.6 is considered highly angular. The results of the permeability test are shown in Figure 3-9 below.

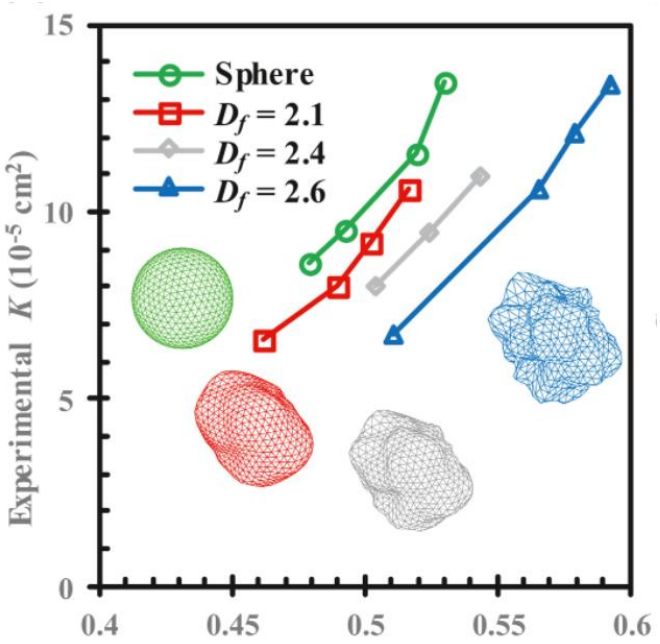

Figure 3- 9 Permeability of Round, and Irregularly 3D Printed Soil Grains and the Effect of Grain Shape on Permeability (Wei et. al, 2021)

The results of the study performed by (Wei et. al, 2021) showed that particle shape does influence the permeability of coarse-grained soils. Their study proposed a modified Kozeny-Carman equation that includes a more in depth calculation of the specific surface area of particle grains based on their particle shape. This study, along with the study performed by Hanoar et. al (2016), are excellent examples of the implementation of additive manufacturing in the geotechnical field. While both studies were successful in their efforts to describe the behavior of soils, the use of a resin-based material has limitations in measuring the strength characteristic of soils (Hanoar et. al, 2016).

A study performed by Jiang et. al. (2020) utilized 3D printing technology to investigate preferential flow through fractured rocks. The leading motivation to additively manufacture gypsum rock was to determine if the anisotropy or isotropy of the fracture surface is governed by the mineral orientation of the fracture and show how that impacts the flow through such fractures. This study printed surrogate rock specimens with varying orientations of bassanite relative to gypsum layers. Unlike the studies performed by Wei et. al (2020) and Hanoar et. al (2016), this study did not implement the use of resin-based printing medium. Fractures were then propagated by a typical three-point bending test, where the load applied to each specimen created a displacement of 10% of the total specimen length. The 3D manufactured rocks with associated tensile fractures were investigated based on the fracture topology, mineral fabric orientation, and then flow through the tensile fractures. They were able to determine that, regarding permeability, the surface roughness of the induced fractures impacts the coefficient of permeability. This study, thus far, has been the closest attempt to use geological type printing medium. Using a similar printing medium to the material found in natural gypsum rock proved to be successful in generating relationships based on mineral fabric orientation, and its impact on fracture properties, as well as the permeability through those fractures.

The final study discussed in this section closely resembles some of the motivations of this study. A study performed by Gomez et. al. (2019) applied additive manufacturing while using soil particles, such as silica sand, as the raw material. They sought to determine if this printing method, and printing medium, was reasonable for investigating the behavior of natural rocks, for the benefit of hydrocarbon recovery methods. Cylindrical cylinders were printed using binder jet technology with the ExOne M-FLEX system. The printing process involved using a silica sand as the printing medium, and Furfuryl alcohol was used as the binder. Consolidated triaxial tests and permeability

tests were performed using Xiameter PMX-200 Silicone Fluid 100CS as the permeant- for permeability test, pore pressure fluid, and the confining pressure fluid. Consolidated triaxial tests were performed under effective confining pressures of 10MPa, 18 MPa, and 25 MPa, and some results of these tests are shown in Figure 3-10.

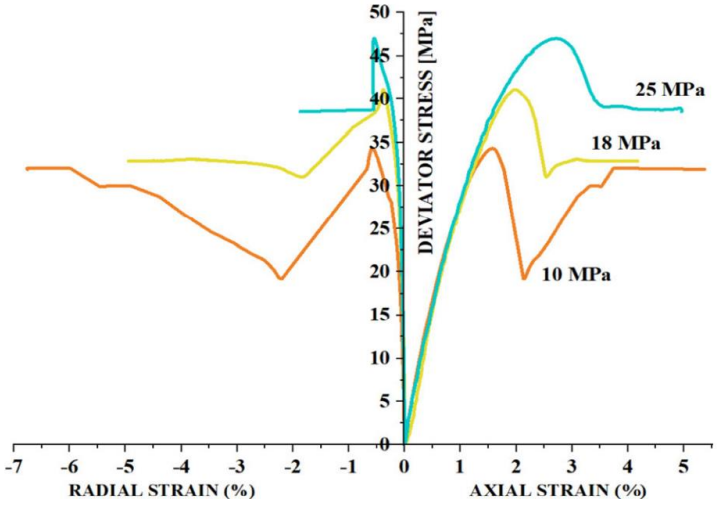

Figure 3- 10 Consolidated Triaxial Tests Performed on 3D Printed Sandstone Specimens (Gomez et. al, 2019)

The results of the triaxial tests were consistent with the behavior found in natural reservoir rocks. However, deviations in the behavior of natural rocks and the 3D printed sandstone specimens were noted from investigations in the compressibility of the printed specimens. Permeability tests were also performed on the sandstone specimens at varying confining stresses, shown in Figure 3-11.

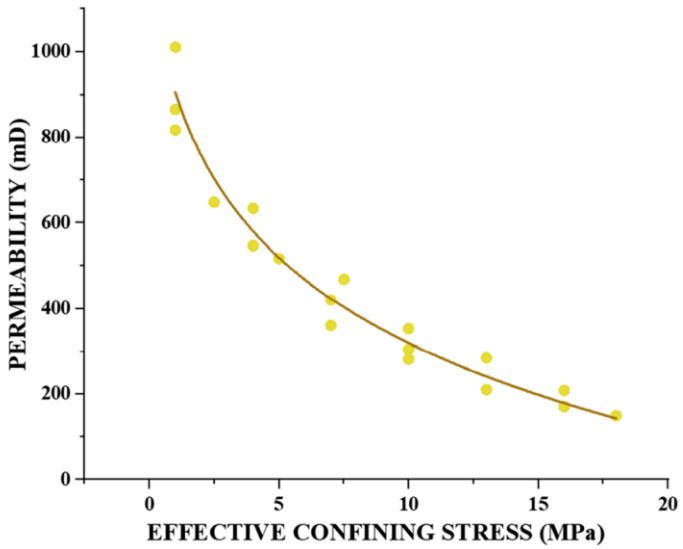

Figure 3- 11 Permeability of 3D Printed Sandstone Specimens (Gomez et. al, 2019)

Permeability of the printed specimens compared well to previously studied natural reservoir rocks, such as Berea sandstone and Fontainebleu sandstones, which are high porosity natural sandstones. They determined that 3D printed sandstone specimens are useful in some investigations of high porosity natural rocks, such as peak shear strength and permeability, but differ in material sensitivity and compressibility. They recommend further studies be performed on decreasing the porosity of 3D printed specimens, which is achieved by either raising or lowering the binder content during the printing process, in an effort to decrease compressibility.

CHAPTER 4

MATERIALS AND TESTING PROCEDURES

4.1 Testing Material Properties

Selecting a representative material to be used for printing is a difficult task due to physical limitations of the printer. This is a common theme in direct binder jet printing, as shown in previous research using similar techniques (Lv et. al, 2019). Ultimately, a commercially available kaolinite stoneware powder, designed for sintering applications, was used for the printing in this research. The stoneware clay is a mostly Kaolin clay with low swelling index and with a measured specific gravity of 2.55, a plasticity index of 7, a liquid limit of 26, and a plastic limit of 19. The chemical composition of the clay powder is outlined in Table 1 and was provided by Tethon 3D.

Table 4- 1 Chemical Composition of Clay-Based Powder for 3D PrintingF

Material	%	Material	%
Fire clay	15-30	Ceramic Frit	3-8
Quartz	10-25	Sodium silicate	2-5
Tectosilicate	5-15	Silica, Cristobalite	2-5
Hydrous Aluminum Silicate	5-15	Silica, amorphous	2-5
Aluminosilicate	5-10	Calcium Aluminate Cement	2-5

More specific chemical identity is withheld by the manufacturer, which may have negligible impact on the printing process. Using complementary sieve and hydrometer analyses, the material was determined to be a low plasticity clay (CL) based on Unified Soil Classification System (USCS), and the result of combined sieve and hydrometer analysis performed in this study is shown in Figure 4-1.

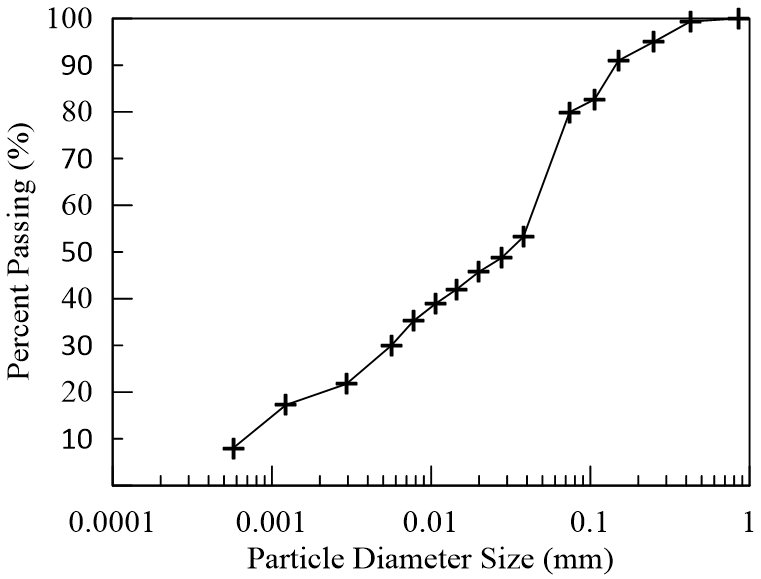

Figure 4- 1 Particle Size Distribution for Clay Powder by Sieve and Hydrometer Analysis

4.2 3D Printing Procedures

3D printed specimens were prepared at the University of Utah using the Exone Innovent + printer – a direct binder jet printer with the capability to print various parts using a number of printing materials. As previously discussed, a binder material must be used during the direct binder jet printing process, and the associated binder was provided by the manufacturer, ExOne, and is the CleanFuse Binder BC001. It is important to note, the binder used in this study is specific only to the printer involved in the printing process. Meaning, the content of the binder is not customizable to the material used, and is a factor of the mechanical inner workings of the 3D printer, and is used with all printing medium.

The direct binder jet printing process would take approximately 24 hours to produce three individual specimens, and this does not include the sintering phase which is discussed in the latter part of this section. Printing the clay cylinders, shown in Figure 4-2, relies on drawings performed

in AutoCAD, and in this case to produce cylinders with 1.4” diameter and 2” in height. The specimen dimensions were determined due to the limitations of the physical powder bed, and the limitations needed to perform permeability tests. It is typically recommended that flexible wall permeameter tests, which are performed on the 3D specimens, should have a ratio of length to diameter equivalent to two. However, the maximum height of the printer only allowed for a 2” specimen, and the flexible wall permeameter located at the University of New Hampshire has a minimum diameter of 1.4”. Thus, the specimen geometry was selected due to these parameters.

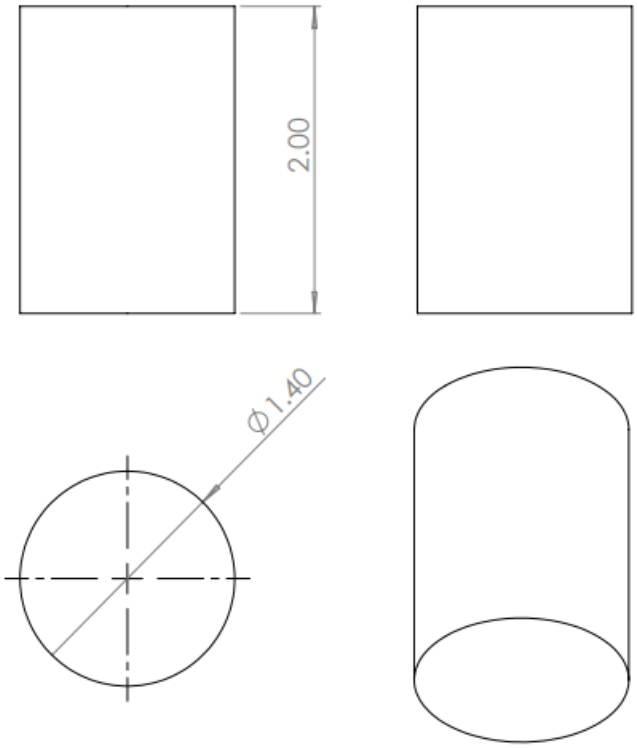

Figure 4- 2 Specimen Geometry for 3D Printing

Dealing with clay material came with its unique set of challenges. Clay has the ability to adsorb water molecules, even moisture from the atmosphere, as discussed in Chapter 2. It is important to note that the ExOne Innovent+ printer is a closed system, and observing the printing

process is difficult, so each step within the feasibility methodology is done in sequence. The initial printing trials using the stoneware clay powder were nearly successful, however, there were deformities during the deposition of the initial layer of clay powder. This was believed to be due to the adsorption of water from the atmosphere, thus, the clay powder was dried in an oven for 10 hours at 200 degrees Celsius. This preliminary procedure successfully increased flowability, and the process was moved into the next stages.

The oven dried clay powder was then placed in the printer hopper, where the powder is deposited into the powder bed. The powder that is deposited within the powder bed is then compressed with a roller to form flat "sheets" of clay powder at the powder bed at a total thickness of 50um per layer. This stage is most affected by the flowability parameter of the powder. Once the powder is sufficiently compressed and rolled, an extrusion nozzle places binder in the geometry of the printed specimens. 1073 total layers of powder with binder between each layer were printed in the powder bed in sequence until the geometry provided by the STL drawing, using AutoCAD was complete. This process produces a "green body" specimen, meaning that the printed specimen is still considered the clay powder with binder at the prescribed saturation ratio, or ratio of binder to powder. Successful prints were produced using the printing parameters shown in Table 4-1.

Table 4- 2 Printing Parameters for Clay Specimens using ExOne Innovent + Printer

Parameters	
Ultrasonic intensity (%)	100
Drying time (sec)	1
Recoat speed (mm/sec)	10
Roller speed (rpm)	250
Roller Traverse speed (mm/sec)	7
Saturation level (%)	48
Packing density (%)	5

The final process of producing a 3D printed clay specimen involves the curing and binder extrusion procedure. This process, initially involved, quickly heating the green body specimens to a temperature of 482° C, the recommended temperature required for binder extrusion and is referred to as the sintering process. However, this process was not without its own challenges. Due to the nature of this study, and the motivation of exploring permeability through intact specimens, and eventually specimens with a predefined fracture geometry, homogeneity within the specimen is especially important. As shown in Figure 4-3 multiple trials of the sintering process were conducted. The initial sintering procedure effectively burned the outer portion of the specimen and did not produce an evenly distributed cured specimen. Subsequent attempts to sinter the specimens included heating the green body specimen to a temperature of 1242° C over a period of 8 hours, where fractures along the printing layers were produced. This method was also unsuccessful.

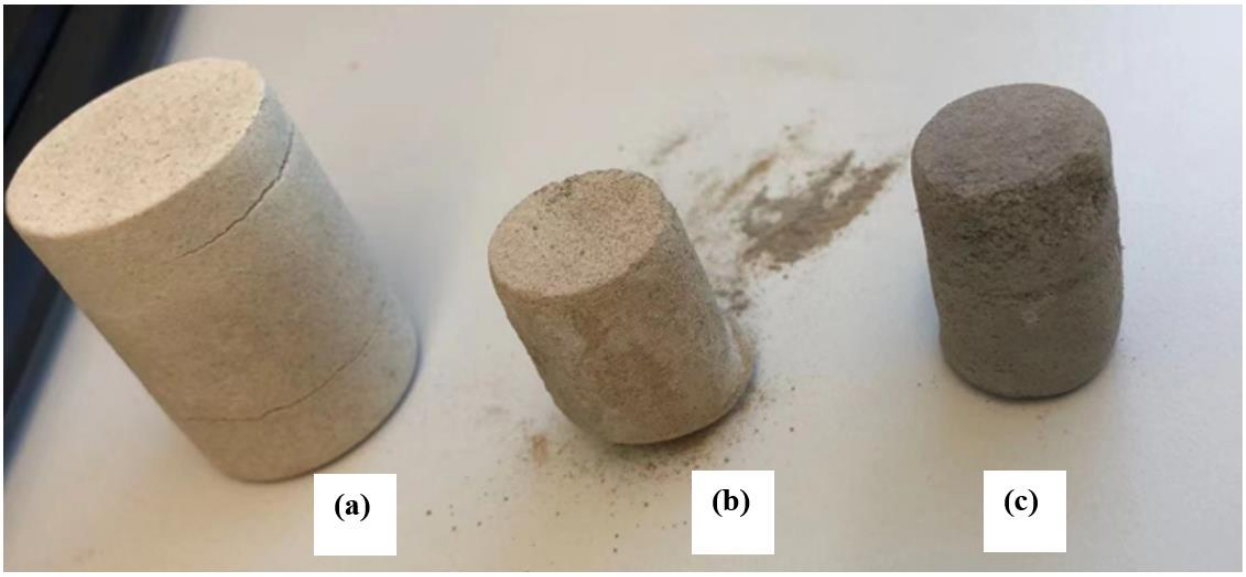

Figure 4- 3 Sintering Results for (a) Sintering to 1242° C (b) Before Sintering (c) Sintering to 284° C

Eventually, the appropriate procedure was conservatively determined to involve heating the green body specimen to using a multi-stage technique. The green body specimens were initially heated from room temperature to 300° C at a rate of 1°C/min, and held at this temperature for 8 hours, then heated to 482° C at the same rate and, again, held at this temperature for 8 hours. The final sintering stage was conducted by heating the specimens from 482° C to 1092°C at the same rate, and then again held at this temperature for 8 hours and brought down to room temperature before extraction. Figure 4-4 shows the first successful print produced by the University of Utah, and achieved a void ratio of 1, that is important for control specimen preparation.

Figure 4- 4 Successful Print of Clay Powder

Similar studies such as the one by Klosek-Wawrzyn et. al. (2013) also showed that high temperature during sintering impacts the behavior of kaolinite clay. In manufactured clays, such as the stoneware clay powder, additives are used to ensure the sinterability of the powder to discourage deformation by shrinkage during the sintering process. Their study also showed that adding a fire- resistant material, such as fireclay and other materials found in the stoneware powder, not only decreases shrinkage during sintering, but also will increase porosity of the specimens. Thus, the saturation ratio of the binder to clay powder content is insufficient to determine the porosity of the material. However, further X-Ray Diffraction (XRD) was also performed on an intact 3D specimen to determine the real porosity of 3D printed specimen. Figure 4-5 displays an image provided by XRD where porosity was determined to be at 0.5, or a void ratio of 1 for the printed specimens in this study, where the porosity was determined using Dragonfly PRO. This procedure involved selecting various scans throughout the depth of the specimen, applying a color filter to the solid particles and no color to the areas denoted as “air”. The ratio of the solid particles to the air particles was used to determine the void ratio.

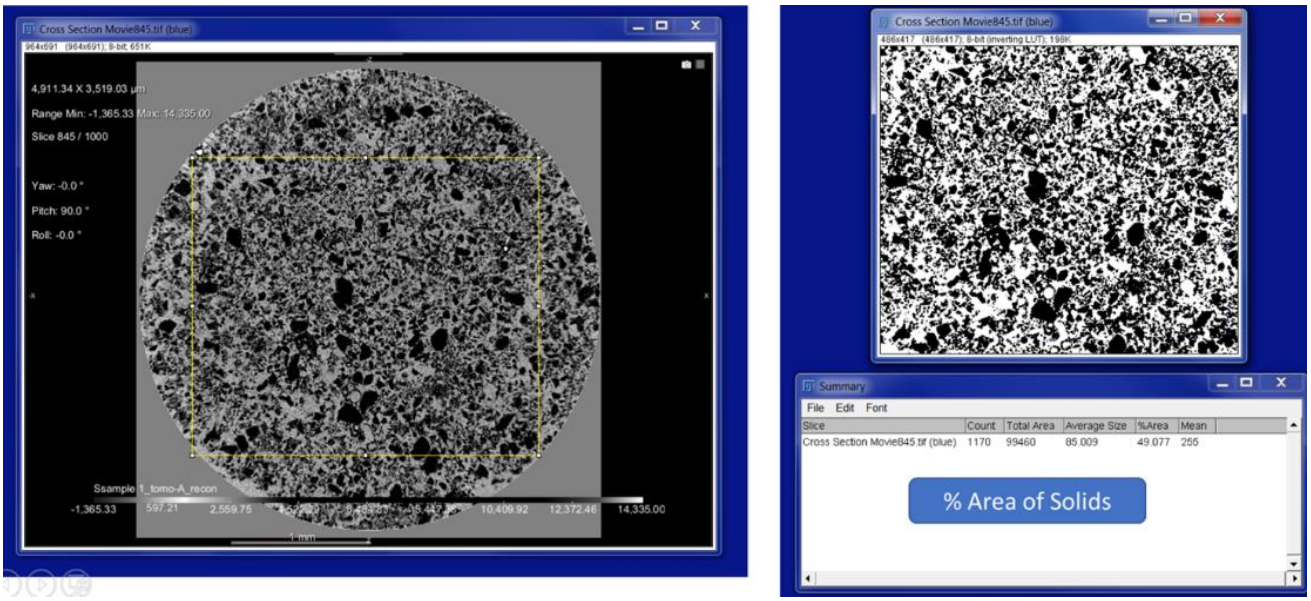

Figure 4- 5 3D Specimen Porosity Determination using Dragonfly PRO Software from XRM

4.3 Flexible Wall Permeability Sample Preparation

To test the effects of 3D printing on clay permeability, it is necessary to test the clay powder used in this study at all stages of the printing process. Thus, clay powder, sintered clay powder without the presence of a binder, and 3D printed specimens were tested in the flexible wall permeameter. Each specimen type with their associated sample preparation, were prepared in the flexible wall permeameter according to their ability or resistance to deformation.

Remolded clay specimens refer to preparation of the clay powder used in printing, in the state at which it is sold by its manufacturer. To have fewer lurking variables during the permeability testing phase, the remolded specimens were prepared as closely as possible to the 3D printed specimen geometry and water content, thus an initial water content of 0% was determined to produce the most reasonable data for comparison, as well as a void ratio of 1. Initial steps to prepare any of the specimens include the following. Two porous stones were brought to a boil in

water to rid the stones of entrapped air, and two filter paper discs were cut to the size of the porous stone at 1.4”. The bottom pedestal, on which the specimen is built, has an associated groove in which an o-ring rests to secure a flexible membrane and prevent leakage, this groove is lubricated with a small amount of vacuum grease to ensure a proper seal. The test cell is equipped with various tubes that allow fluid flow through the top and bottom of the specimen. The presence of air within a permeability test can impact the results of that test, thus, each line was flushed with de-aired water prior to each test, and the valves were closed to ensure no air could enter the system. At this point, specimen construction is ready to begin.

Remolded specimens were prepared in a manner that is similar to the dry-pluviation of coarse-grained material. However, because the remolded specimens are not prepared to a specific relative density, it is more reasonable to denote this process as “placing” clay powder within a cylindrical mold. For the purposes of this procedure, pluviation may be used to effectively communicate the procedures within. After the initial preparation stages of the test cell were complete, a porous stone and filter paper were placed on the bottom pedestal. A membrane stretcher, applied to a vacuum, was then used to place the membrane around the bottom pedestal and secured with an O-ring. The membrane stretcher was then removed at which point a split cell mold was placed around the membrane and bottom pedestal, with vacuum applied, and the top unsecured side of the membrane was folded over the membrane stretcher to ensure the membrane was flush to the split mold. 50g of dry clay powder used for printing, was then pluviated into the mold atop the porous stone and filter paper, using a wide-mouthed funnel and brought to a height of 2”. Filter paper was placed on a porous stone, and placed within the membrane atop the clay powder with the filter paper in contact with the clay. The top cap was then placed on the porous stone, and secured with an O-ring. At this point, the sample preparation method was successful.

However, upon removing the split cell mold, the sample deformed greatly due to the following stages. A test cell was then place around the specimen, where confining stress is applied via de-aired water, and the top platen is placed atop the test cell, and the piston is placed within a groove located on the top cap of the specimen. Due to the stiffness of the lines that are connected from the top cap to the bottom platen, coupled with the placement of the piston onto the top cap, great deformation was observed during this stage. Thus, the subsequent procedures involved placing a wire mesh cylinder around the specimen after the split cell mold was removed, and before the tubing to the top cap was attached. Additionally, to decrease deformation during this stage, the tubing from the top cap was lengthened, cut, and fittings were placed to attach the tubes to the top cap after the mesh was installed. Figure 4-6 below shows the remolded specimen with the associated cage, and added tube fittings. At this point, the specimen was successfully placed within the test cell, and filled with de-aired water.

Figure 4- 6 Remolded Clay Specimen Preparation with Grid Mesh and Tube Modifications

Sintering the clay powder was conducted at the University of New Hampshire. Approximately 90 g of clay powder were placed within a highly heat resistant ceramic container, with dimensions of 2.2” in top diameter, 2” for the bottom diameter, and 2.4” in height. The clay powder within the ceramic container was then placed in an oven and sintered using the same procedure described for sintering the green body specimens. The specimens were then removed from the container, and were brought to the geometry as the remolded and 3D printed specimens by lightly sanding the excess clay from the specimen.

Sample preparation for the 3D printed and sintered specimens was much simpler in terms of preparing the test cell than the remolded specimens. 3D printed specimens were also tested under the same conditions in the triaxial cell set up. Reconstituting 3D specimens was not required for testing; thus, the cylindrical printed specimens were placed on the bottom pedestal atop a porous stone and filter paper, and secured to the top cap and bottom pedestal with a membrane and two O-rings.

4.4 Flexible Wall Permeability Test Procedures

Permeability tests were performed using the GeoComp Fully Automated Flow Trac II, as discussed in Chapter 2. The system was prepared for testing by filling each pump; cell, bottom pressure, and top pressure, with de-aired water. The pumps were then emptied and filled again three consecutive times to ensure no air was present in the system, by observing the de-aired water tank for air bubbles traveling through the system. The top pump, or permeability pump, was then filled with de aired water to 15% capacity, and the cell pump and bottom pressure pump were filled to 80% capacity. The permeability test cell was then placed in the load frame and brought to a height such that the locked piston was approximately one centimeter below the LVDT sensor. Tubing associated with each pump, that is eventually connected to the test cell, was secured near the test cell at heights equivalent with the center of the specimen, for the cell pressure line, and the top and bottom of the specimen for the top and bottom pressure lines, respectively. During this time, the sensors associated with each pump were calibrated to read 0 kPa pressure at these heights, and then connected to the test cell as shown in Figure 4-7.

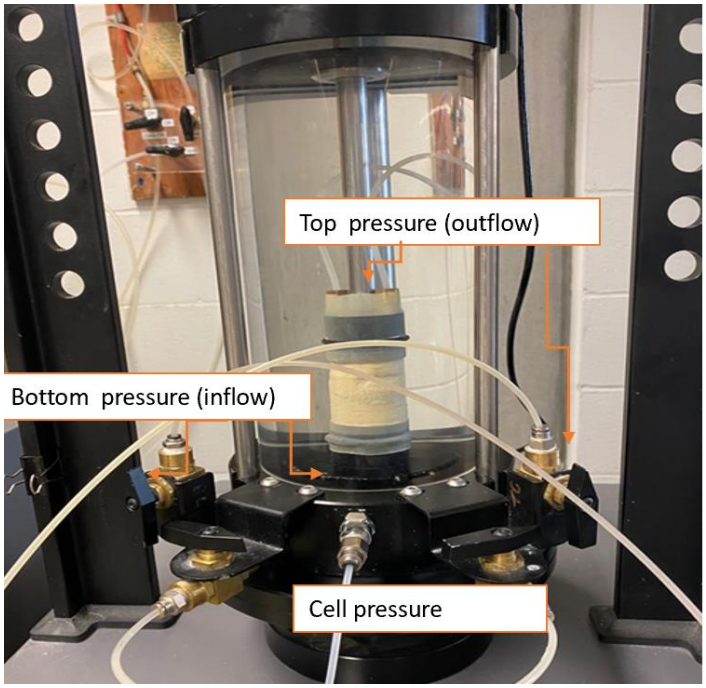

Figure 4- 7 Flexible Wall Permeameter Test Cell Set Up

These tests were executed in three stages of saturation, consolidation, and constant gradient permeability (ASTM D5084-16a). De-aired water was used as the confining pressure and flow media. Permeability tests were conducted on four 3D printed specimens at confining pressures of 5, 10, and 20 kPa, respectively, as well as three remolded clay specimens, and three sintered specimens. The constant gradient permeability test was performed in five steps to determine the lowest gradient possible to achieve flow and was determined to be a gradient of 5 for printed specimens. Remolded specimens were performed under a hydraulic gradient of 2, as these specimens were much softer and more likely to be affected by higher hydraulic gradients during permeability. A small confining stress of 3 kPa was applied to the specimens during an initialization stage prior to saturation, to ensure over-consolidation did not occur for any test specimens. The initialization stage was performed to ensure no leaks were occurring between the

test cell and the specimen. Upon completion of the initialization stage, the saturation, consolidation, and permeability stages were performed in sequence. Saturation was performed using back-pressure saturation and was considered complete at a B-value of approximately 0.95 or higher for all specimens. Saturation was performed at a pressure increment of 20 kPa with a pressure rate of 0.5 kPa per second. Consolidation was performed with an effective horizontal vertical stress of 5, 10, and 20 kPa to mimic shallow conditions of naturally deposited clays. The fully automated capabilities of the triaxial set up allowed for sequential testing of permeability at different confining stresses on the same specimen. Specimens tested at 10 kPa and 20 kPa were first tested at the lower confining stresses, and then consolidated at the higher confining stresses to determine permeability and for comparability of results.

CHAPTER 5

EXPERIMENTAL RESULTS AND DISCUSSION

5.1 Effect of 3D Printing Process on Soil Properties

From visual and tactile observations, it became apparent that the 3D printing process affected the physical characteristics of the clay material. Most notably, the 3D printed specimens appeared to have a very high stiffness, and a rougher surface. Thus, a preliminary study of the potential chemical changes to the material was conducted as well as the physical changes due to the 3D printing and sintering. Specimens that were printed were evaluated for physical properties including Atterberg limits, particle size gradation, and specific gravity. Sieve analysis performed on pulverized 3D printed specimens would result in different distribution and are unreasonable to perform accurately as the pulverization technique is difficult to repeat. However, hydration was attempted on 3D printed specimens to determine if Atterberg limits could reasonably be performed. Upon soaking the 3D printed specimens in deaired water for 24 hours, pulverizing by hand, Atterberg limits were attempted. Notably, Atterberg limits on pulverized 3D printed specimens could not be conducted, leading to the conclusion that the stoneware clay powder may no longer be nominally classified as a cohesive material due to 3D printing effects. To better understand these changes both from chemical composition standpoint and at micro level, scanning election microscopy (SEM) and energy dispersive x-ray spectroscopy (EDS) were also performed.

SEM was conducted on both 3D printed specimens as well as remolded and unprocessed stoneware clay powder in an effort to determine changes in particle structure, a factor that will affect permeability as discussed in Chapter 2. Further, SEM imaging proved to be useful in visualizing the physical changes of the clay, and the effect of printing on the particle configuration.

Figure 5-1 shows the distinct change in particle structure of the clay powder before and after printing. Although the figure associated with the 3D printed specimen was analyzed intact, and not pulverized, it is apparent that the smaller platy structures of Kaolin clay are less common post printing. Additionally, the particle shapes of the 3D printed specimens appear to have drastically changed during the printing and sintering process, where the highly irregular particle shape appears to have some smooth surfaces and angular edges unlike the unprocessed clay.

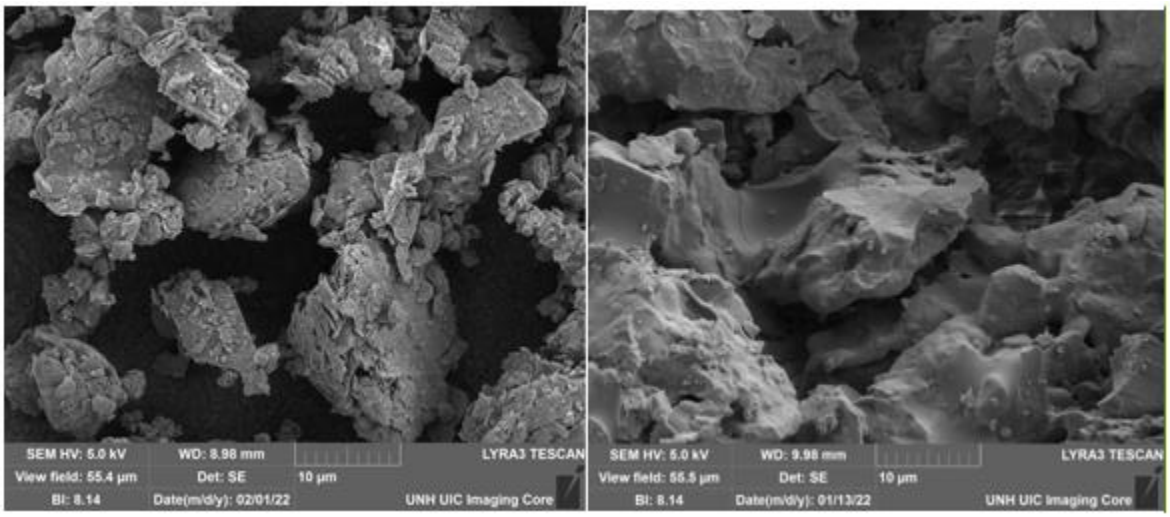

Figure 5- 1 SEM Imaging of Remolded Clay (left) and 3D Printed Clay (right)

Tangentially, the effects of sintering process alone on clay was investigated to determine further, the effect of binder evacuation on the physical properties of the clay. Thus, the SEM Imaging was also conducted on the sintered clay specimens as shown in Figure 5-2. The imaging of the sintered clay more closely resembles the characteristics of the 3D printed clay. A similar smooth surface with some angular edges is discovered as well, the presence of individual particles or particles typical of Kaolinite clay- such as a platy shaped particle, are also lacking in the sintered photos.

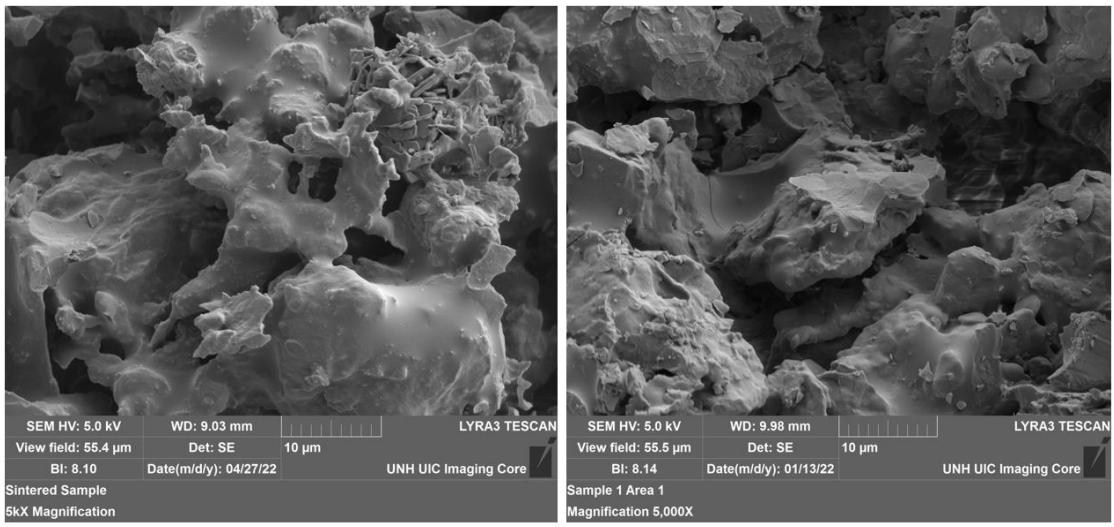

Figure 5- 2 SEM Imaging of Sintered Clay (left) and 3D Printed Clay (right)

Similar studies such as the one by Klosek-Wawrzyn et. al. (2013) also showed that high temperature during sintering impacts the behavior of Kaolinite clay. Phase changes occur during the sintering phase of the clay powder, and 3D prints associated with chemical reactions governed by temperature (Klozek-Wawrzyn et. al, 2013). On such chemical reaction, termed the "glassy phase" is demonstrated in Figure 5-2 as the clay particles appear to melt together. In manufactured clays, such as the stoneware clay powder, additives are used to ensure the sinterability of the powder to discourage deformation by shrinkage during the sintering process. This study also showed that adding a fire- resistant material, such as fireclay and other materials found in the stoneware powder, not only decreases shrinkage during sintering, but also will increase porosity of the specimens.

Scanning electron microscopy (SEM) was conducted on both 3D printed specimens as well as remolded and unprocessed stoneware clay powder, in junction with energy dispersive x-ray spectroscopy (EDS), in an effort to determine changes in particle structure and determine if

residual binder were the driving factor in the changes in plasticity and particle shape. EDS analysis was conducted to determine if significant changes in carbon content of the material were apparent that indicate the presence of residual binder not evacuated during the sintering process. Figure 5-3 displays the results of EDS analysis using the commercially available Tescan Lyra3 GMU FIB SEM, by the University of New Hampshire Instrumentation Center. The data show that little change in carbon content was detected, and it was reasonable to assume that all binder was evacuated from the 3D printed specimens. While the content of the binder has been successfully evacuated during the curing and sintering process for the 3D printed specimens, it is reasonable to note that the chemical reactions between the binder and the material during sintering will impact the 3D printed specimens, in terms of permeability. A third control specimen is introduced during the permeability stage of this investigation, to determine the effect of sintering on the permeability of clay that is discussed in the latter portion of this chapter. Nevertheless, it is reasonable to assume that the printing and sintering process have contributed to the changes in physical properties of the material.

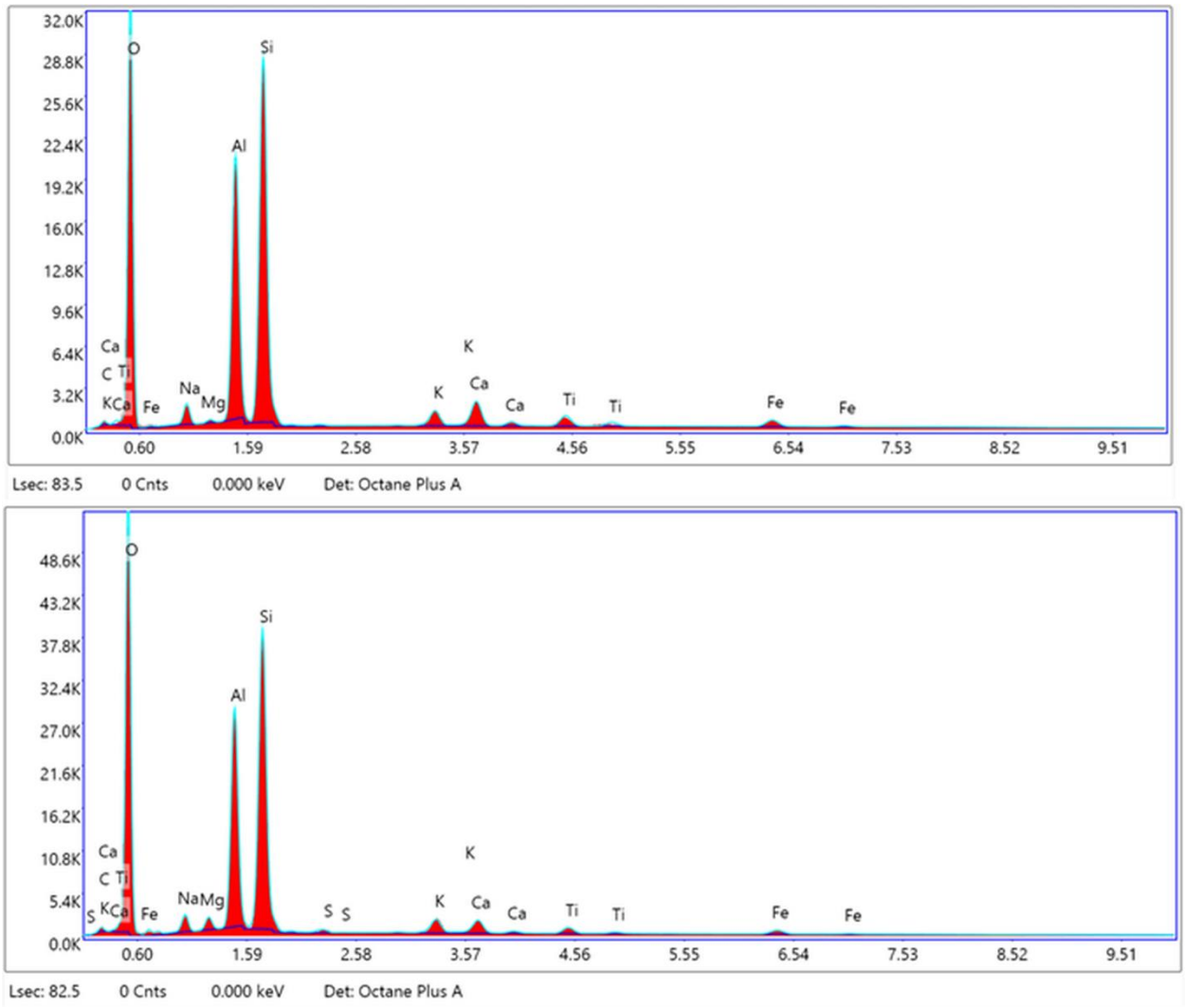

Figure 5- 3 EDS analysis of both printed (top) and clay powder (bottom)

5.2 Effects of 3D Printing on Clay Permeability

The saturated permeability of 3D printed specimens ranged from $1.2*10^{-1}$ cm/s to $7.7*10^{-4}$ cm/s at confining pressures ranging from 5 to 20 kPa. The permeability of the sintered specimens at the same effective confining pressures ranged from $7.8*10^{-4}$ cm/s to $4.76*10^{-4}$ cm/s. Finally, the permeability of remolded specimens, however, ranged from $4.45*10^{-5}$ cm/s to $5.56*10^{-6}$ cm/s at the same confining pressures. While all specimens were saturated to a B-value

of at least 0.95, 3D printed and sintered specimens achieved a B-Value of 0.97 or higher where remolded specimens ranged from 0.95-0.96. The saturation ratio is well known to influence the saturated hydraulic conductivity of soils (Chapuis et. al, 2012), and this variation should be noted for the purpose of this study. The permeability of the 3D printed specimens is significantly higher than that of the remolded specimens under the same confining pressures as shown in Figure 5-4. Notably, the variations in permeability of the remolded specimens are more apparent than the 3D printed specimens. It is reasonable to conclude that the remolded specimens are far more sensitive to external movement than the 3D printed specimens, where the printed specimens are much stiffer than the remolded specimens. Additionally, the permeability of the sintered specimens, while typically lower, most closely resembles the permeability of the 3D printed specimens. Permeability decreases more as confining pressure increases for remolded specimens, a behavior that relates to the deformability of the remolded specimens. 3D printed specimens are much stiffer, followed by the sintered specimens, than remolded specimens and will resist effective pressures with a lower reduction in void ratio as those pressures increase. It is reasonable then, to conclude that the effect of the binder in the 3D printed specimens largely contributes to the stiffness and particle shape of the clay, as well as the increased stiffness. While sintered specimens were very stiff, they appeared to less stiff than the 3D printed specimens. Triaxial tests would be most appropriate to perform in an effort to gain a full understanding of the total effects of 3D printing on mechanical response of these clay. However, for the purposes of this study, only permeability was investigated, and any observations related to the strength of the specimens is based on general observations during sample preparation.

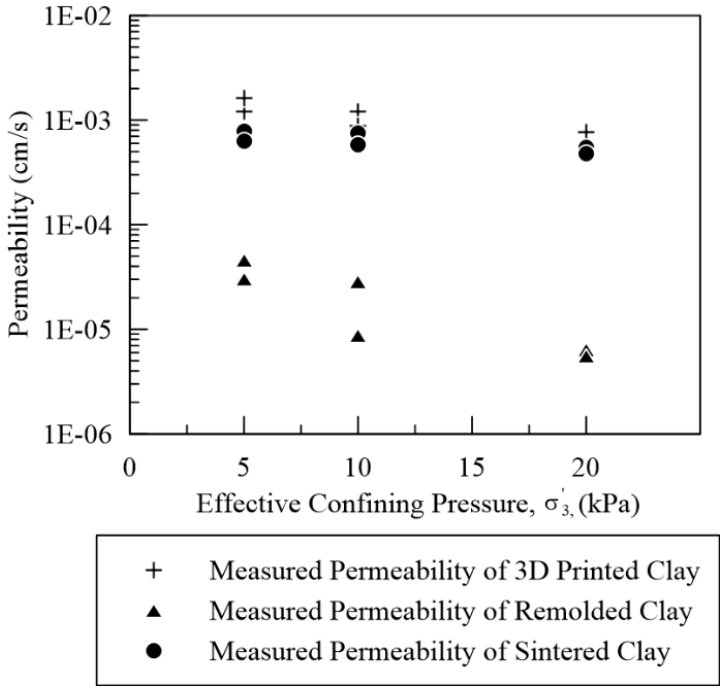

Figure 5- 4 Effect of confining pressure on the permeability of 3D printed and remolded clay specimens

The use of empirical equations to estimate the permeability of 3D printed, sintered, and remolded specimens are especially helpful in determining the application of geo-manufacturing to studies in soil mechanics. A variation of the Kozeny-Carman equation, Equation 2-14, was implemented to calculate the permeability of the 3D printed, sintered, and remolded specimens according to their plasticity, specific surface area, and density. The specific surface area for the remolded specimens was determined by applying equations proposed by Chapuis and Legare (1992) in Equation 2-9, where $P_{No\,D} - P_{No\,d}$ is defined as the percentage by weight smaller than size D and the next larger particle size than the investigated size, d.

For the remolded specimens, Equation 2-14 was initially applied to determine the specific surface area of the clay particles; however, this relationship yielded a permeability of at least 4 orders of magnitude smaller than the measured permeability. Therefore, using Equation 2-9 (similar to printed and sintered specimens) was a much better estimation of permeability in terms

of the materials sieve analysis, over its plasticity index. The application of the K-C equation with specific area determination proposed by Chapuis et. al (2003) appears to be a good fit for 3D printed and sintered specimens, shown in Figure 5-5. Estimations of permeability from specific surface data by (Foth, 1978) show that the permeability of the 3-D printed specimens lies within the estimated permeability for fine to medium sands. The variability of permeability at each confining pressure for the remolded specimens is greater than that of the 3D printed and sintered specimens. At 10 kPa, the K-C formulation appears to be a good fit for the remolded specimens. The 3D printed, sintered, and remolded specimens demonstrate decreasing permeability with increasing confining pressure, a relationship to be expected (Taylor et. al, 1948; Mesri and Olson, 1971; Samshiringhe et. al, 1982; Chapuis et. al 2004).

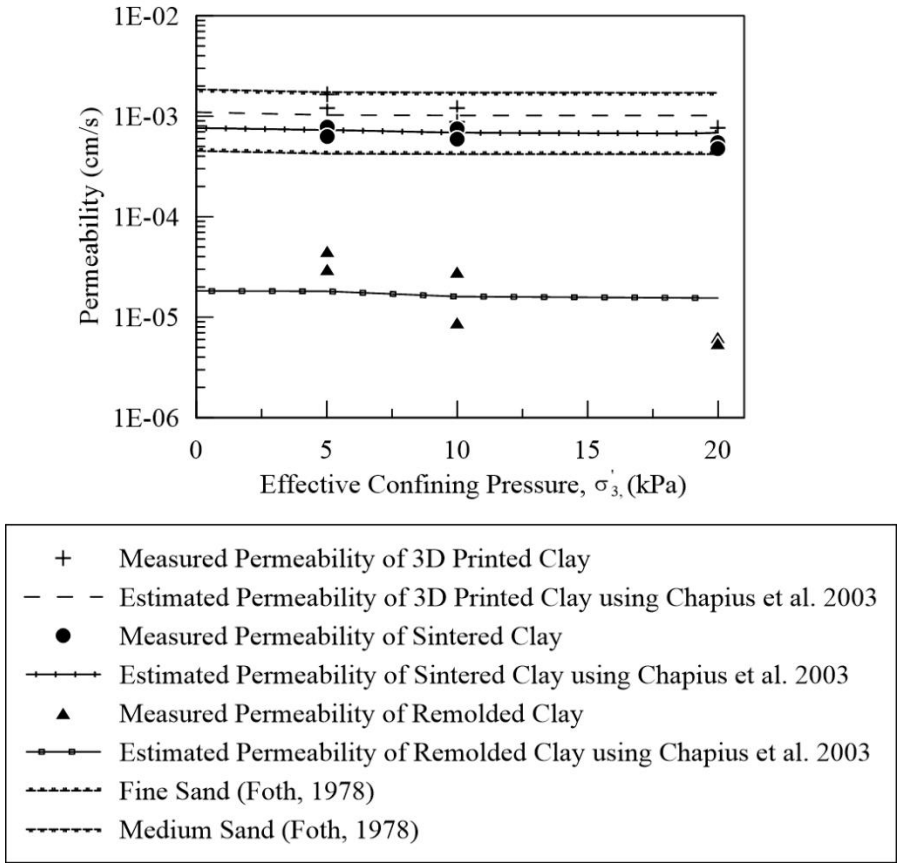

Figure 5- 5 Effect of confining pressure on the permeability of 3D printed and remolded clay specimens with the relationship proposed by Chapuis et. al. (2003)

Decreasing permeability for both remolded specimens and 3D printed specimens appears to be a function of the effective confining pressure impacting the void ratio, as shown in Equation 2-14. The effect on confining pressure versus permeability has varying effects on the 3D printed, sintered, and remolded specimens. A figure demonstrating this effect is shown in Figure 5-6.

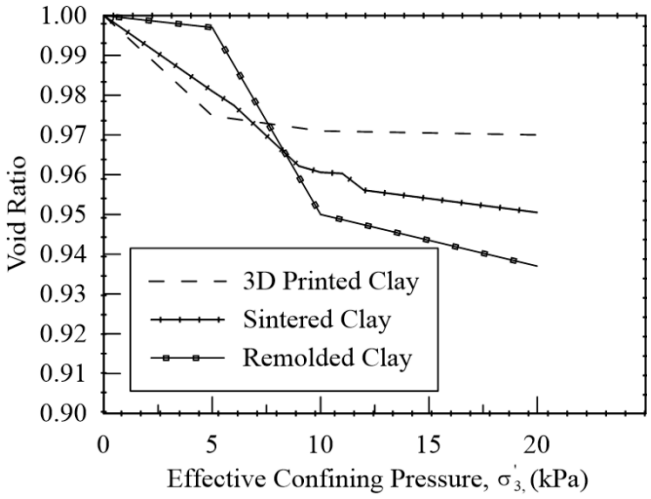

Figure 5- 6 Effect of Confining Pressure on Void Ratio for 3D Printed, Sintered, and Remolded Specimens

Thus, to further determine the impact of confining pressure on void ratio as well as permeability, the measured permeability values were normalized to the function of the void ratio in Equation 2-7; i.e., the function at which void ratio was normalized to is shown in Equation 5-1.

$$f(e) = \frac{e^3}{1+e} \qquad (5\text{-}1)$$

The normalization of the actual permeability values, shown in Figure 5-7**,** indicates that the void ratio does impact the permeability of each specimen as the extent of the variation decreased.

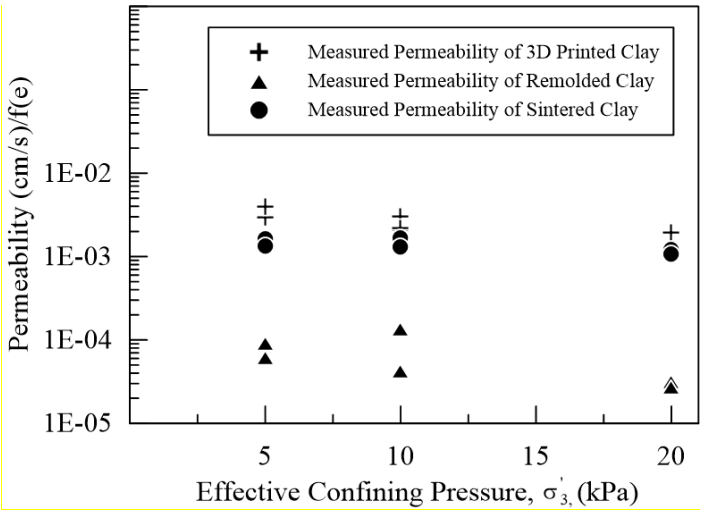

Figure 5- 7 Permeability of 3D printed and remolded clay specimens normalized to void ratio function

The impact on such change is especially notable for the remolded specimens, where the decreasing trend in permeability as effective confining stress increases is less apparent in the normalized data. Thus, the remolded specimens are much more responsive to the effects of confining pressure in terms of permeability due to the decreasing void ratio, as pore spaces close and limit the available volume for fluid flow. However, the effective confining pressure still influences the permeability even without its effect on void ratio. This can be attributed to an approximate nature of Equation 5-1. During the investigation of the physical changes of the clay due to 3D printing, the specific gravity was determined to be the same for both printed and remolded specimens. Therefore, the specific gravity will not impact the permeability of the remolded specimens due to 3D printing. The final impact of 3D printing on clay permeability is certainly the influence on the particle size and shape of the material. SEM images displayed notable changes in particle shape and orientation after 3D printing, as well as after sintering. The increase

in permeability, according to the K-C equation, can also be attributed to the decrease in the specific surface area.

CHAPTER 6

CONCLUSIONS AND FUTURE WORKS

6.1 Conclusions

A series of flexible wall permeameter tests were performed on 3D printed specimens, sintered specimens, and remolded specimens at effective confining pressures of 5kPa, 10kPa, and 20kPa. The fully automated system measures permeability in three stages, saturation, consolidation, and constant gradient permeability. Investigations into the changes of clay powder due to direct binder jet printing were conducted by the use of SEM, EDS, and XRM. The results of these investigations are outlined below.

- Measurable physical changes occur during the 3D printing of manufactured clay used in this study; most notably, the plasticity and changes to specific surface area. The elimination of plasticity during the sintering process is likely to increase measured permeability of the 3D printed specimens compared to the remolded specimens. It is very likely that the change in plasticity due to printing and increasing the specific surface area promoted a higher permeability in the 3D printed specimens than the remolded specimens.
- XRM and SEM imaging led to the observation that it is likely that the physical changes of the specimens do occur during the sintering phase, and have in turn, made a cohesive material non-cohesive. This leads to interesting opportunities to investigate the applicability of a printing process that has little effect on the EDL of cohesive materials as well as the particle size.

- There is greater observed stiffness in the 3D printed specimens which likely allows them to be more resistant to confining pressure than remolded specimens, which are very soft.
- Specimen deformation and disturbance is less likely to occur during sample preparation of many procedures using 3D printed specimens.
- Variability in permeability measurements is greater in the remolded specimens than the 3D printed specimens and varies largest at very low confining pressures of 5 kPa. A concluded benefit to geo-manufacturing soil specimens is evident in the permeability results of this study by reducing variability in void ratio in soil specimens to determine a more reliable measurement of permeability.
- Estimating permeability using empirical correlations, such as the Chapuis extension to the Kozeny-Carman equation fit well with 3D printed specimens, and can be useful in preliminary design of 3D printed specimens.
- 3D printing will increase the permeability of clay specimens prepared at the same porosity, as the specific surface area increases, cohesion is eliminated, and stiffness is increased.
- 3D printing will be beneficial in implementing a fracture geometry into clay specimens, as sample deformation is less likely to occur due to the fracture in 3D printed specimens, and nearly impossible to do in remolded specimens.

Overall, there is a distinct benefit in leveraging additive manufacturing to investigate flow through soils. Variations in permeability that are frequently caused by sample preparation are less present in the 3D printed specimens, a certain benefit to 3D printing in permeability investigations. A low hydraulic gradient can be applied to 3D printed specimens, where achieving the lowest possible

hydraulic gradient at a certain confining pressure is imperative to performing reasonable testing. Also, it would be beneficial to produce a fracture geometry into the 3D printed specimens and systematically investigate the flow characteristics. Although this study revealed the challenges involved with 3D printed specimens resembling the target clay, achieving repeatable models, low stress-induced deformations, and potential for architected fracture networks make 3D printing an appealing sample preparation alternative.

6.2 Future Works

Advances in additive manufacturing have been impactful on the investigation of soil behavior, as outlined in this thesis. While this study was able to adequately print clay material using direct binder jet printing, the process in which the clay is printed and sintered for curing impacted the material such that permeability of 3D printed clays is much higher than remolded clay specimens of the same void ratio, confining stresses, and geometry. 3D printing technology is a relatively new technology and has only been implemented in studies for the past decade or so, specifically in direct binder jet printing. There are multiple areas in which the technology itself can improve to better provide specimens that are representative of fine-grained soils. However, this would require research in the material sciences as well, as clay powder designed for printing. Largely, the greatest impact the printing process has on soil is the sintering process, therefore, it would be most successful for the study of clay materials to eliminate this binder evacuation technique altogether, such a process is unreasonable to suggest regarding the technology.

Future work should also include the triaxial testing of remolded, sintered, and 3D printed clays. This study could not reasonably perform these tasks given the time constraints of the research, and printing scheduling at the University of Utah. However, it would be most beneficial to determine the effects the printing process has on the strength characteristics of the clay material

and determine how the printed and sintered specimens behave under triaxial conditions. It is the recommendation of this thesis that consolidated undrained triaxial tests be performed on the specimens at effective confining pressures of 5kPa, 10kPa, and 20kPa. It is reasonably to hypothesize that the 3D printed specimens will have the highest shear strength, with sintered specimens following, and remolded specimens as the weakest. Additionally, it would be beneficial to investigate an equality in effective confining pressures to shear strength between the remolded specimens and the 3D printed specimens to determine if there is an effective confining pressure at which the 3D specimens will behave similarly to the clay specimens. Such research could benefit in the further evaluation of the effects of 3D printing on clay, but also may prove to be useful in the investigation of preferential flow through fractured surfaces. Thus, this study finally recommends that the 3D printed specimens be tested at much higher confining pressures to determine if there are any confining pressures that permeability will resemble that of the remolded specimens. At present, the void ratio at which specimens are prepared are set by the capabilities of the ExOne Innovent+ printer, and the binder saturation percentage, and is also impacted by shrinkage occurring during the sintering process. However, there may be a void ratio due to applied effective confining pressure that negates the effect of the change in particle size on permeability, that can provide a better investigation in the permeability of fractured clays. Most importantly, it is the belief of this research that a fracture geometry should be printed in clay specimens. Thin rectangular fracture geometries printed horizontally, vertically, and at varying angles would be beneficial to investigate preferential flow through macropores. The difficulty in implementing a controlled fracture in remolded fine-grained specimens makes it nearly impossible to do without deformation, and even more difficult to do an enclosed fracture system. 3D printing would implement only a small outlet, large enough to insert a small vacuum suction to remove clay

material that has not been injected with binder in the fracture, and then subsequently sintered and tested. Remolded specimens would be unable to achieve such a confinement, and the fracture would likely be open to the flexible membrane during testing.

LIST OF REFERENCES

Alaoui, A., et al. “A Review of the Changes in the Soil Pore System Due to Soil Deformation: A Hydrodynamic Perspective.” *Soil and Tillage Research*, vol. 115-116, 2011, pp. 1–15., https://doi.org/10.1016/j.still.2011.06.002.

Bockhorn, Britta, et al. “Factors Affecting the Hydraulic Performance of Infiltration Based Suds in Clay.” *Urban Water Journal*, vol. 14, no. 2, 2015, pp. 125–133., https://doi.org/10.1080/1573062x.2015.1076860.

Campbell, Graylon. “How to Measure Specific Surface of Soil with the WP4C.” *Meter Environment*, https://library.metergroup.com/Sales%20and%20Support/METER%20Environment/Website%20Articles/measure-specific-surface-soil-wp4c.pdf.

Carman, P C. “Fluid Flow through a Granular Bed.” *Transactions of the Institution of Chemical Engineers*, 1937, pp. 150–167.

Chapuis, Robert P, and Michel Aubertin. “On the Use of the Kozeny–Carman Equation to Predict the Hydraulic Conductivity of Soils.” *Canadian Geotechnical Journal*, vol. 40, no. 3, 2003, pp. 616–628., https://doi.org/10.1139/t03-013.

Chapuis, Robert P. “Predicting the Saturated Hydraulic Conductivity of Soils: A Review.” *Bulletin of Engineering Geology and the Environment*, vol. 71, no. 3, 2012, pp. 401–434., https://doi.org/10.1007/s10064-012-0418-7.

Chapuis, Robert P. “Predicting the Saturated Hydraulic Conductivity of Soils: A Review.” *Bulletin of Engineering Geology and the Environment*, vol. 71, no. 3, 2012, pp. 401–434., https://doi.org/10.1007/s10064-012-0418-7.

Chapuis, Robert P. “Similarity of Internal Stability Criteria for Granular Soils.” *Canadian Geotechnical Journal*, vol. 29, no. 4, 1992, pp. 711–713., https://doi.org/10.1139/t92-078.

Chen, Qirong, et al. “Binder Jetting Process with Ceramic Powders: Influence of Powder Properties and Printing Parameters.” *Open Ceramics*, vol. 9, 2022, p. 100218., https://doi.org/10.1016/j.oceram.2022.100218.

Chen, Zhangwei, et al. “3D Printing of Ceramics: A Review.” *Journal of the European Ceramic Society*, vol. 39, no. 4, 2019, pp. 661–687., https://doi.org/10.1016/j.jeurceramsoc.2018.11.013.

Chiangka, Saowaluk, et al. “Effect of Slurry Formulation on Morphology and Flowability of Spray-Dried Alumina/Zirconia Composite Particles.” *Key Engineering Materials*, vol. 675-676, 2016, pp. 531–534., https://doi.org/10.4028/www.scientific.net/kem.675-676.531.

Christ, Susanne, et al. “Fiber Reinforcement during 3D Printing.” *Materials Letters*, vol. 139, 2015, pp. 165–168., https://doi.org/10.1016/j.matlet.2014.10.065.

Daniel, DE, et al. “Fixed-Wall versus Flexible-Wall Permeameters.” *Hydraulic Barriers in Soil and Rock*, 1985, https://doi.org/10.1520/stp34573s.

Das, Braja M., and N. Sivakugan. *Principles of Foundation Engineering*. 8th ed., Cengage Learning, 2017.

Deckers, Jan, et al. “Additive Manufacturing of Ceramics: A Review.” *Journal of Ceramic Science and Technology*, vol. 5, no. 4, 2014, pp. 245–260.

Di Prima, Simone, et al. “Detecting Infiltrated Water and Preferential Flow Pathways through Time-Lapse Ground-Penetrating Radar Surveys.” *Science of The Total Environment*, vol. 726, 2020, p. 138511., https://doi.org/10.1016/j.scitotenv.2020.138511.

Dolinar, B, et al. “Liquid Limit and Specific Surface of Clay Particles.” *Geotechnical Testing Journal*, vol. 27, no. 6, 2004, p. 11325., https://doi.org/10.1520/gtj11325.

Dolinar, Bojana. “Predicting the Hydraulic Conductivity of Saturated Clays Using Plasticity-Value Correlations.” *Applied Clay Science*, vol. 45, no. 1-2, 2009, pp. 90–94., https://doi.org/10.1016/j.clay.2009.04.001.

Dreelin, Erin A., et al. “A Test of Porous Pavement Effectiveness on Clay Soils during Natural Storm Events.” *Water Research*, vol. 40, no. 4, 2006, pp. 799–805., https://doi.org/10.1016/j.watres.2005.12.002.

Feenstra, F K. “Method for Making a Dental Element.” 2005.

Fooladm, Hamid. “Estimating Soil Specific Surface Area Using the Summation of the Number of Spherical Particles and Geometric Mean Particle-Size Diameter.” *African Journal of Agricultural Research*, vol. 6, no. 7, 2011, pp. 1758–1762.

Gomez, J. S., et al. “Experimental Investigation of the Mechanical Behavior and Permeability of 3D Printed Sandstone Analogues under Triaxial Conditions.” *Transport in Porous Media*, vol. 129, no. 2, 2018, pp. 541–557., https://doi.org/10.1007/s11242-018-1177-0.

Hanaor, D. A., et al. “3D Printable Geomaterials.” *Géotechnique*, vol. 66, no. 4, 2016, pp. 323–332., https://doi.org/10.1680/jgeot.15.p.034.

Hazen, Allen. “XXIII. Some Physical Properties of Sands and Gravels, with Special Reference to Their Use in Filtration.” *State Sanitation Volume II*, 1892, https://doi.org/10.4159/harvard.9780674600485.c25.

Holtz, R. D., et al. *An Introduction to Geotechnical Engineering*. 2nd ed., Pearson Education, Inc., 2011.

Hvorslev, M. Juul. *Time Lag and Soil Permeability in Ground-Water Observations*. U.S. Army Corps of Engineers, 1951.

Ishai, I, et al. “Concept and Test Method for a Unified Characterization of the Geometric Irregularity of Aggregate Particles.” *Journal of Testing and Evaluation*, vol. 5, no. 1, 1977, p. 3., https://doi.org/10.1520/jte10529j.

Jallo, Laila J., et al. “The Effect of Surface Modification of Aluminum Powder on Its Flowability, Combustion and Reactivity.” *Powder Technology*, vol. 204, no. 1, 2010, pp. 63–70., https://doi.org/10.1016/j.powtec.2010.07.017.

Jiang, Liyang, et al. “Mineral Fabric as a Hidden Variable in Fracture Formation in Layered Media.” *Scientific Reports*, vol. 10, no. 1, 2020, https://doi.org/10.1038/s41598-020-58793-y.

Klint, Knud Erik, and Peter Gravesen. “Fractures and Biopores in Weichselian Clayey till Aquitards at Flakkebjerg, Denmark.” *Hydrology Research*, vol. 30, no. 4-5, 1999, pp. 267–284., https://doi.org/10.2166/nh.1999.0015.

Kozłowski, Rafał, et al. “Zooremediation of Leachates from Municipal Waste Using Eisenia Fetida (Sav.).” *Environmental Pollution*, vol. 254, 2019, p. 112871., https://doi.org/10.1016/j.envpol.2019.07.039.

Kłosek-Wawrzyn, Ewelina, et al. “Sintering Behavior of Kaolin with Calcite.” *Procedia Engineering*, vol. 57, 2013, pp. 572–582., https://doi.org/10.1016/j.proeng.2013.04.073.

Lamb, S. *Soil Mechanics*, 1969, pp. xi-xii., https://doi.org/10.1017/cbo9780511815553.002.

Lefevbre, A. 2021. "Permeafor Testing of Granular SoilsThesis, Civil and Environmental Engineering, University of New Hampshire, Durham, NH.

Lewis, Jennifer A., et al. “Direct Ink Writing of Three-Dimensional Ceramic Structures.” *Journal of the American Ceramic Society*, vol. 89, no. 12, 2006, pp. 3599–3609., https://doi.org/10.1111/j.1551-2916.2006.01382.x.

Li, Chunguang. “Void Ratio–Permeability Relations for Clays.” *Quarterly Journal of Engineering Geology and Hydrogeology*, vol. 53, no. 2, 2019, pp. 298–303., https://doi.org/10.1144/qjegh2018-158.

Li, Liangxing, and Weimin Ma. “Experimental Study on the Effective Particle Diameter of a Packed Bed with Non-Spherical Particles.” *Transport in Porous Media*, vol. 89, no. 1, 2019, pp. 35–48., https://doi.org/10.1007/s11242-011-9757-2.

Loiselle, A, and J Hurtubise. “Properties and Behavior of till as Construction Material.” 1976.

Loudon, A. G. “The Computation of Permeability from Simple Soil Tests.” *Géotechnique*, vol. 3, no. 4, 1952, pp. 165–183., https://doi.org/10.1680/geot.1952.3.4.165.

Lv, Xinyuan, et al. “Binder Jetting of Ceramics: Powders, Binders, Printing Parameters, Equipment, and Post-Treatment.” *Ceramics International*, vol. 45, no. 10, 2019, pp. 12609–12624., https://doi.org/10.1016/j.ceramint.2019.04.012.

McBrayer, M. C., et al. “Infiltration Tests on Fractured Compacted Clay.” *Journal of Geotechnical and Geoenvironmental Engineering*, vol. 123, no. 5, 1997, pp. 469–473., https://doi.org/10.1061/(asce)1090-0241(1997)123:5(469).

Mesri, Gholamreza. “Mechanisms Controlling the Permeability of Clays.” *Clays and Clay Minerals*, vol. 19, no. 3, 1971, pp. 151–158., https://doi.org/10.1346/ccmn.1971.0190303.

Moore, R. “The Chemical and Mineralogical Controls upon the Residual Strength of Pure and Natural Clays.” *Géotechnique*, vol. 41, no. 1, 1991, pp. 35–47., https://doi.org/10.1680/geot.1991.41.1.35.

Nebelung, M, and B Lang. “Flowability of Ceramic Bulk Materials Part 2: Interaction of Primary Particle Properties and Flowability.” *Ceramic Forum International*, vol. 86, 2009.

Ordoñez, Edisson, et al. “3D Printing via the Direct Ink Writing Technique of Ceramic Pastes from Typical Formulations Used in Traditional Ceramics Industry.” *Applied Clay Science*, vol. 182, 2019, p. 105285., https://doi.org/10.1016/j.clay.2019.105285.

Pap, Miklós, and András Mahler. “Comparison of Different Empirical Correlations to Estimate Permeability Coefficient of Quaternary Danube Soils.” *Periodica Polytechnica Civil Engineering*, 2018, https://doi.org/10.3311/ppci.13108.

Powrie, William. *Soil Mechanics: Concepts and Applications*. E & FN Spon, 1997.

Ren, Xingwei, et al. “A Relation of Hydraulic Conductivity — Void Ratio for Soils Based on Kozeny-Carman Equation.” *Engineering Geology*, vol. 213, 2016, pp. 89–97., https://doi.org/10.1016/j.enggeo.2016.08.017.

Revelo, Carlos F., and Henry A. Colorado. “3D Printing of Kaolinite Clay Ceramics Using the Direct Ink Writing (DIW) Technique.” *Ceramics International*, vol. 44, no. 5, 2018, pp. 5673–5682., https://doi.org/10.1016/j.ceramint.2017.12.219.

Revelo, Carlos F., and Henry A. Colorado. “3D Printing of Kaolinite Clay Ceramics Using the Direct Ink Writing (DIW) Technique.” *Ceramics International*, vol. 44, no. 5, 2018, pp. 5673–5682., https://doi.org/10.1016/j.ceramint.2017.12.219.

Samarasinghe, A. Mahinda, et al. “Permeability and Consolidation of Normally Consolidated Soils.” *Journal of the Geotechnical Engineering Division*, vol. 108, no. 6, 1982, pp. 835–850., https://doi.org/10.1061/ajgeb6.0001305.

Sander, Per. “Lineaments in Groundwater Exploration: A Review of Applications and Limitations.” *Hydrogeology Journal*, vol. 15, no. 1, 2006, pp. 71–74., https://doi.org/10.1007/s10040-006-0138-9.

Schmitz, Robrecht M. “Can the Diffuse Double Layer Theory Describe Changes in Hydraulic Conductivity of Compacted Clays?” *Geotechnical and Geological Engineering*, vol. 24, no. 6, 2006, pp. 1835–1844., https://doi.org/10.1007/s10706-005-3365-2.

Schriever, William. “Law of Flow for the Passage of a Gas-Free Liquid through a Spherical-Grain Sand.” *Transactions of the AIME*, vol. 86, no. 01, 1930, pp. 329–336., https://doi.org/10.2118/930329-g.

Shahzad, Aamir, and Ismail Lazoglu. “Direct Ink Writing (DIW) of Structural and Functional Ceramics: Recent Achievements and Future Challenges.” *Composites Part B: Engineering*, vol. 225, 2021, p. 109249., https://doi.org/10.1016/j.compositesb.2021.109249.

Slichter. vol. 19, U.S. Geological Survey, 1899, pp. 2–305, *Theoretical Investigation of the Motion of Ground Waters*.

Smale, Stevanovic, and Chavanne P. “Improvement of Mechanical Properties of 3D Printed Hydroxyapatite Scaffolds by Polymeric Infiltration.” *Bioceramics Development and Applications*, vol. 3, no. s1, 2013, https://doi.org/10.4172/2090-5025.s1-012.

Solís Pinargote, Nestor Washington, et al. “Direct Ink Writing Technology (3D Printing) of Graphene-Based Ceramic Nanocomposites: A Review.” 2020, https://doi.org/10.20944/preprints202004.0409.v1.

Spillmann, Adrian, et al. “Flowability Modification of Lactose Powder by Plasma Enhanced Chemical Vapor Deposition.” *Plasma Processes and Polymers*, vol. 4, no. S1, 2010, https://doi.org/10.1002/ppap.200730202.

Suwanprateeb, J., et al. “Influence of Printing Parameters on the Transformation Efficiency of 3d-Printed Plaster of Paris to Hydroxyapatite and Its Properties.” *Rapid Prototyping Journal*, vol. 18, no. 6, 2012, pp. 490–499., https://doi.org/10.1108/13552541211272036.

Tagliaferri, S., et al. “Direct Ink Writing of Energy Materials.” *Materials Advances*, vol. 2, no. 2, 2021, pp. 540–563., https://doi.org/10.1039/d0ma00753f.

Tang, Shiyan, et al. “Direct Ink Writing Additive Manufacturing of Porous Alumina-Based Ceramic Cores Modified with Nanosized Mgo.” *Journal of the European Ceramic Society*, vol. 40, no. 15, 2020, pp. 5758–5766., https://doi.org/10.1016/j.jeurceramsoc.2020.07.058.

Taylor, Donald W. *Fundamentals of Soil Mechanics*. Chapman and Hall, 1948.

Travitzky, Nahum, et al. “Additive Manufacturing of Ceramic-Based Materials.” *Advanced Engineering Materials*, vol. 16, no. 6, 2014, pp. 729–754., https://doi.org/10.1002/adem.201400097.

Wei, Deheng, et al. “Permeability of Uniformly Graded 3D Printed Granular Media.” *Geophysical Research Letters*, vol. 48, no. 5, 2021, https://doi.org/10.1029/2020gl090728.

Wilsey, Edward Franklin, and Frederic Theodore Mavis. “A Study of the Permeability of Sand.” 1936, https://doi.org/10.17077/006163.

Xia, Yuanlin, et al. “Microstructure and Mechanical Property of CF/SIC Core/Shell Composite Fabricated by Direct Ink Writing.” *Scripta Materialia*, vol. 165, 2019, pp. 84–88., https://doi.org/10.1016/j.scriptamat.2019.02.016.

Zhou, B., et al. “Three-Dimensional Sphericity, Roundness and Fractal Dimension of Sand Particles.” *Géotechnique*, vol. 68, no. 1, 2018, pp. 18–30., https://doi.org/10.1680/jgeot.16.p.207.

Zhou, B., et al. “Three-Dimensional Sphericity, Roundness and Fractal Dimension of Sand Particles.” *Géotechnique*, vol. 68, no. 1, 2018, pp. 18–30., https://doi.org/10.1680/jgeot.16.p.207.